

4D-A104 384

AIR FORCE GEOPHYSICS LAB HANSCOM AFB MA  
ROCKET DATA OF SOLAR EUV FLUX, THERMOSPHERIC ELECTRON FLUX, AND ETC(U)

F/G 4/1

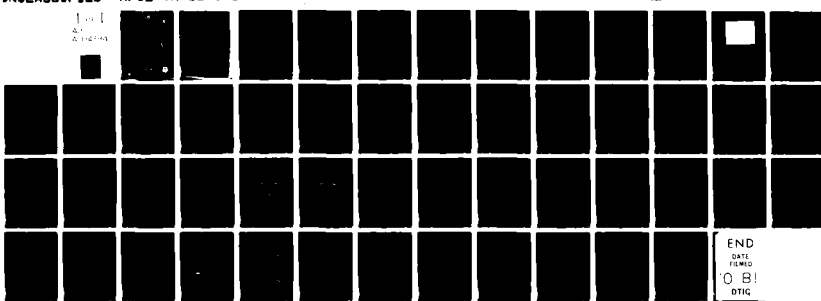
APR 81 R A VAN TASSEL, W J McMAHON, L HEROUX

JNCLASSIFIED

AFGL-TR-81-0111

NL

1000  
A1  
A1-2-1-3



END  
DATE  
FILED  
O B I  
DTIG

AD A104384

LEVEL

14) AFGL-TR-81-0111 AFGL-ERP-737  
ENVIRONMENTAL RESEARCH PAPER NO. 737



12) G  
Rocket Data of Solar EUV Flux,  
Thermospheric Electron Flux,  
and N<sub>2</sub> Second-Positive Airglow Emission.

10)

R. A. VAN TASSEL  
W. J. McMAHON  
L. HEROUX

11)

17 April 1981

12) 52

16) 6694, 17) 16

DTIC  
SELECTED  
SEP 18 1981  
S H

Approved for public release; distribution unlimited.

AERONOMY DIVISION PROJECT 6690  
AIR FORCE GEOPHYSICS LABORATORY  
HANSCOM AFB, MASSACHUSETTS 01731

AIR FORCE SYSTEMS COMMAND, USAF

FILE COPY



409578

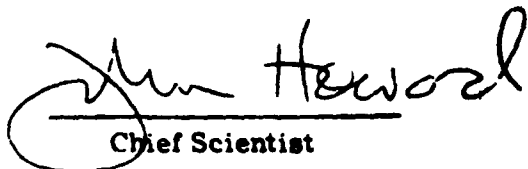
4B

81 9 18 063

This report has been reviewed by the ESD Information Office (OI) and is  
releasable to the National Technical Information Service (NTIS).

This technical report has been reviewed and  
is approved for publication.

FOR THE COMMANDER



John Heward  
Chief Scientist

Qualified requestors may obtain additional copies from the  
Defense Technical Information Center. All others should apply to the  
National Technical Information Service.

**Unclassified**

SECURITY CLASSIFICATION OF THIS PAGE (When Data Entered)

REPORT DOCUMENTATION PAGE		READ INSTRUCTIONS BEFORE COMPLETING FORM
1. REPORT NUMBER <b>AFGL-TR-81-0111</b>	2. GOVT ACCESSION NO. <b>AD-A104 384</b>	3. RECIPIENT'S CATALOG NUMBER
4. TITLE (and Subtitle) <b>ROCKET DATA OF SOLAR EUV FLUX, THERMOSPHERIC ELECTRON FLUX, AND N<sub>2</sub> SECOND-POSITIVE AIRGLOW EMISSION</b>	5. TYPE OF REPORT & PERIOD COVERED <b>Scientific. Interim.</b>	
7. AUTHOR(s) <b>R. A. Van Tassel W. J. McMahon L. Heroux</b>	6. PERFORMING ORG. REPORT NUMBER <b>ERP No. 737</b>	
9. PERFORMING ORGANIZATION NAME AND ADDRESS <b>Air Force Geophysics Laboratory (LKO) Hanscom AFB Massachusetts 01731</b>	10. PROGRAM ELEMENT, PROJECT, TASK AREA & WORK UNIT NUMBERS <b>62101F 66901604</b>	
11. CONTROLLING OFFICE NAME AND ADDRESS <b>Air Force Geophysics Laboratory (LKO) Hanscom AFB Massachusetts 01731</b>	12. REPORT DATE <b>17 April 1981</b>	
14. MONITORING AGENCY NAME & ADDRESS (if different from Controlling Office)	13. NUMBER OF PAGES <b>52</b>	
	15. SECURITY CLASS. (of this report) <b>Unclassified</b>	
	15a. DECLASSIFICATION DOWNGRADING SCHEDULE	
16. DISTRIBUTION STATEMENT (of this Report)  <b>Approved for public release; distribution unlimited.</b>		
17. DISTRIBUTION STATEMENT (of the abstract entered in Block 20, if different from Report)		
18. SUPPLEMENTARY NOTES		
19. KEY WORDS (Continue on reverse side if necessary and identify by block number) <b>Solar EUV flux Thermospheric electron flux N<sub>2</sub> airglow emission</b>		
20. ABSTRACT (Continue on reverse side if necessary and identify by block number) <b>This report presents simultaneous measurements of solar EUV flux, thermospheric photoelectron energy flux, and airglow radiation from the nitrogen second positive band system made from an Aerobee 170 rocket launched from White Sands Missile Range on 14 August 1979 at 2020 UT. The solar EUV data are combined with flux measurements obtained by H. E. Hinteregger with the solar EUV spectrometer on the Atmospheric Explorer-E Satellite to provide flux measurements over the complete range of 51 to 1026 Å.</b>		

DD FORM 1 JAN 73 1473

**Unclassified**

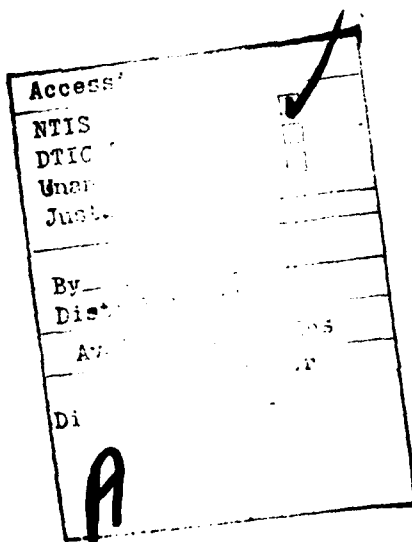
SECURITY CLASSIFICATION OF THIS PAGE (When Data Entered)

**Unclassified**

SECURITY CLASSIFICATION OF THIS PAGE(When Data Entered)

**20. Abstract (Continued)**

The energy range of the electron flux extends from 2.4 to 5.7 eV and from 14 to 34 eV. The airglow emission from the 0, 0 band of the nitrogen second positive system is presented as both volume and column rates. The volume emission rate shows a major broad peak near 150 km and a less intense peak at 108 km.



**Unclassified**

SECURITY CLASSIFICATION OF THIS PAGE(When Data Entered)

## **Preface**

We thank the Naval Ordnance Missile Test Facility at the White Sands Missile Range for assistance in preparation, testing, and launch of the rocket payload. The solar pointing control and telemetry systems were provided by Ball Aerospace Systems Division under the direction of D. F. Bradshaw. Mr. Richard Salter of this laboratory (AFGL) was the Test Conductor. We also thank K. H. Bhavnani of RADEX, Inc. for assistance in the data reduction.

## **Contents**

1. INTRODUCTION	7
2. ROCKET FLIGHT	8
3. SOLAR EUV FLUX MEASUREMENTS	8
3.1 The Spectrometer	10
3.2 Radiometric Calibration of the Spectrometer	12
3.3 The Solar Flux	13
4. ELECTRON SPECTROMETER	20
4.1 Experimental	20
4.2 Results	23
5. NITROGEN SECOND POSITIVE AIRGLOW MEASUREMENTS	25
5.1 The Dayglow Photometer	25
5.2 Calibration of the Photometer	26
5.2.1 The Relative Instrumental Response, $\eta(\lambda)$	27
5.2.2 The Calibration Factor, C	30
5.3 Mechanism of N <sub>2</sub> Second Positive Dayglow	33
5.3.1 The Position of the Rotational Lines	34
5.3.2 The Relative Intensity of the Rotational Lines	35
5.4 Flight Data	36
5.4.1 Volume Emission Rate	46
5.4.2 Column Emission Rate	46
REFERENCES	49

## **Illustrations**

1. Rocket Payload Configuration Showing the Electron Analyzer Mounted on the Rear Surface of the Solar-Pointed EUV Spectrometer and the Airglow Photometer Mounted Below the Spectrometer and Electron Analyzer	9
2. Schematic of the Solar EUV Spectrometer	10
3. The Absorption of the Unresolved Solar Emission Lines of HeII and SiXI at 303.78 and 303.31 Å, Respectively, as a Function of Altitude	21
4. Cross Section of the Electron Energy Analyzer	22
5. The Photoelectron Energy Distribution Between 14 and 34 eV	24
6. The Photoelectron Energy Distribution Between 2.4 and 5.7 eV	25
7. Schematic Diagram of the Dayglow Photometer	26
8. Schematic Arrangement for Determining the Instrument Response Function	28
9. Relative Spectral Response of Channel 0	29
10. Relative Spectral Response of Channel 3	29
11. Relative Spectral Response of Channel 2	30
12. The Spectral Irradiance of the Calibrated Standard Lamp, FEL F056F, at 50 cm	32
13. The Spectral Distributions of Intensity of the 3371 Å Band of the N <sub>2</sub> Second Positive System at Temperatures From 200° to 900°K	37
14. The Relative Band Response for Filter Channels 0 and 3 to the 3371 Å Band of N <sub>2</sub> for Rotational Temperatures Ranging From 200° to 1000°K	41
15. The Elevation of the Photometer During the Flight	42
16. The Azimuth of the Photometer During the Flight	42
17. Counts per 100 msec Frame vs Altitude for Channel 0	43
18. Counts Per 100 msec Frame vs Altitude for Channel 3	43
19. Counts Per 100 msec Frame vs Altitude for Channel 2	44
20. Counts Per 100 msec Frame vs Altitude for Channel 1 (dark count)	44
21. Counts Per 100 msec Frame vs Altitude for Second Positive Emission for Channel 0	45
22. Counts Per 100 msec Frame vs Altitude for Second Positive Emission for Channel 3	45
23. Volume Emission Rate for the N <sub>2</sub> Second Positive (0, 0 band) Emission	47
24. Volume Emission Rate of N <sub>2</sub> Second Positive (0, 0 band)	47
25. Column Emission Rate of N <sub>2</sub> Second Positive (0, 0 band)	48

## Tables

1. Wavelength Regions Covered by Spectrometer	11
2. Solar Flux for 14 August 1979, at 2020 UT	14
3. Channel Parameters	30
4. Characteristics of Each of the Photometer Channels	33
5. Rotational Constants, $B_c$ , for the X, B, and C States of Nitrogen	34
6. Line Strengths for Hund's Case <u>a</u>	35

## **Rocket Data of Solar EUV Flux, Thermospheric Electron Flux, and N<sub>2</sub> Second-Positive Airglow Emission**

### **I. INTRODUCTION**

This report presents data obtained from a single rocket flight in AFGL's Aeronomy Division's program of support of the Defense Meteorological Satellite Program/SSD density sensor. The measurements include the solar extreme ultraviolet (EUV) flux between 51 and 1026 Å, the thermospheric photoelectron flux between 2.4 and 5.7 eV and between 14 and 34 eV, and the dayglow emission from the nitrogen second positive system. The rocket measurement of solar EUV flux covered only limited regions of the wavelength range 50 to 1026 Å. However, the rocket data have been combined with flux measurements obtained by H. E. Hinteregger with the EUV spectrometer on the NASA Atmosphere Explorer (AE)-E satellite to provide flux measurements over the complete range of 51 to 1026 Å. A future report will compare the data reported here for the photoelectron flux and airglow emissions with that computed by using the AFGL ionospheric model developed in AFGL's Space Physics Division.

The parameters measured in the rocket flight are interrelated. The atmospheric absorption of solar EUV radiation is the chief source of production of electrons in the upper atmosphere. The energies of the atmospheric photoelectrons produced by solar UV absorption cover an energy range from approximately 0 to 100 eV. These atmospheric photoelectrons then excite the N<sub>2</sub> second positive

---

(Received for publication 15 April 1981)

bands as well as other emission lines and bands of various atomic and molecular atmospheric species.

For a particular atmospheric density profile and solar EUV spectrum, the AFGL model predicts the electron fluxes as a function of both energy and altitude. These electron fluxes can then be combined with the atmospheric density profile to predict the intensity of those atmospheric emissions that are excited solely by electron impact excitation. The purpose of the rocket experiment was to obtain simultaneous measurements of solar EUV flux, photoelectron energy flux, and airglow radiation from the nitrogen second positive band system to verify the model, and, therefore, determine if atmospheric density profiles can be determined remotely from a satellite by observing optical emissions from the earth's upper atmosphere.

## 2. ROCKET FLIGHT

The rocket payload was flown in an Aerobee 170 rocket from White Sands Missile Range, New Mexico, on 14 August 1979 at 2020 UT. The peak altitude of the rocket was 178 km. Data were obtained during rocket ascent and descent. The payload configuration is illustrated in Figure 1. The solar EUV spectrometer was mounted on a biaxial pointing control that pointed the spectrometer at the center of the solar disk. The electron energy analyzer was mounted on the rear surface of the EUV spectrometer so that the analyzer aperture remained in a sun-shaded position and aligned nearly parallel to the geomagnetic field lines throughout the period of data acquisition. The N<sub>2</sub> airglow photometer was mounted in a separate section below the solar spectrometer but above the azimuth joint of the biaxial pointing control. Its pointing direction was determined by means of a Miniature Inertial Digital Attitude System (MIDAS).

## 3. SOLAR EUV FLUX MEASUREMENTS

In this section, measurements of solar EUV fluxes in the wavelength region from 51 to 1026 Å incident on top of the earth's atmosphere are presented. One scan of the wavelength region 51 to 306 Å and several scans of the four emission lines of FeXV at 284.15 Å, HeII at 303.78 Å, OV at 629.73 Å, and SiIII at 1206.52 Å were obtained during the rocket flight. These limited rocket data are combined with data from the solar EUV experiment on the Atmosphere Explorer (AE)-E satellite to provide measurements of solar flux over the complete wavelength range 51 to 1026 Å. This wavelength region is the chief source of ionization in the thermosphere. The AE-E measurements that were obtained close in

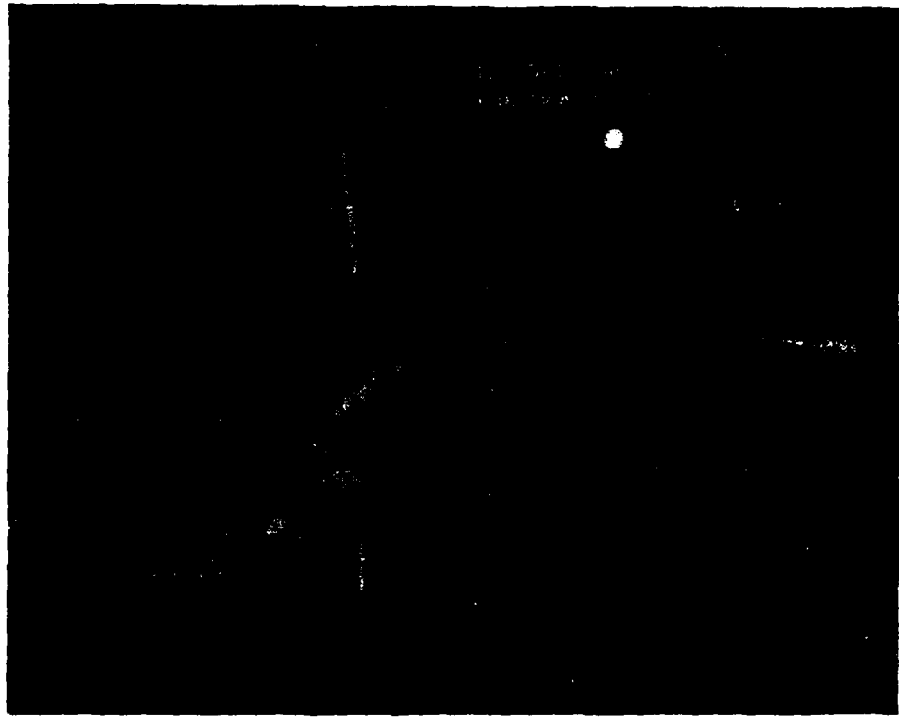


Figure 1. Rocket Payload Configuration Showing the Electron Analyzer Mounted on the Rear Surface of the Solar-Pointed EUV Spectrometer and the Airglow Photometer Mounted Below the Spectrometer and Electron Analyzer

time to those of the rocket measurements cover the range 140 to 1800 Å. The rocket measurements, therefore, provide data in the region 51 to 140 Å that is not covered by the AE-E spectrometer. In addition, the high spectral resolution measurements of the rocket experiment were used to calibrate the AE-E spectrometer.

The purpose of measuring the altitude dependence of the four emission lines given above was to determine the densities of the neutral atmospheric constituents N<sub>2</sub>, O<sub>2</sub>, and O by measuring the absorption coefficients of the lines as a function of altitude.<sup>1</sup> However, meaningful densities could not be obtained with this method in the present experiment. As pointed out by Higgins,<sup>1</sup> an error of 10 percent in the values of either the absorption coefficients of the emission lines

1. Higgins, J. E. (1976) The solar EUV flux between 230 and 1220 Å on November 9, 1971, J. Geophys. Res. 81:1301.

or the cross sections of the atmospheric constituents can introduce an error of a factor of 2 in the densities of  $N_2$  and O. In addition to errors in the cross sections, the errors in the determination of the absorption coefficients of the lines for the present experiment were also subject to relatively large errors because of the large magnitude of the atmospheric absorption of the solar UV lines due to the low peak altitude (178 km) of the rocket and the high exospheric temperature ( $1245^{\circ}\text{K}$ ) for the time of the flight.

### 3.1 The Spectrometer

A schematic of the rocket UV spectrometer is given in Figure 2. The instrument consists of two grazing incidence spectrometers fabricated from a single casting. The entrance slits and concave gratings are clamped against reference surfaces that position them on the Rowland circles located one above the other. Gold coated replica gratings having a radius of curvature of 2 m and a blaze angle of  $4^{\circ}$  are illuminated at an angle of incidence of  $86^{\circ}$  from the grating normal.

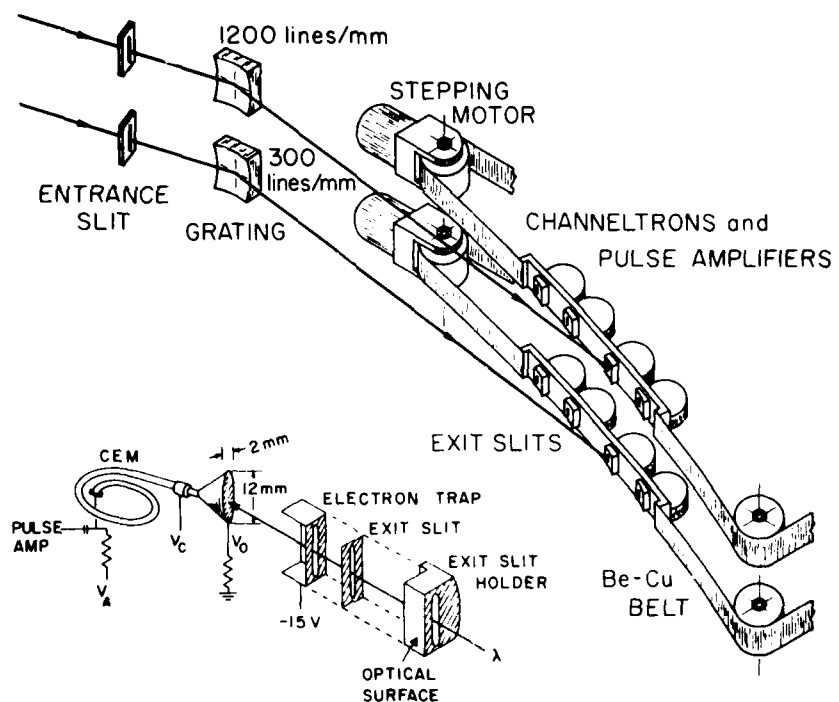


Figure 2. Schematic of the Solar EUV Spectrometer. The inset illustrates the assembly of each exit slit and its Galileo channel electron multiplier. The optical surfaces on each exit slit holder and on the entrance slit holders, not shown, are used to align the exit and entrance slits for parallelism

For wavelength scanning, the four exit slits located on each Rowland circle are moved in small steps along the circle with a stepping motor. The exit slits on each deck are coupled together so that each slit covers a limited wavelength region during flight, as summarized in Table 1. For the deck equipped with a 1200 line/mm grating, the four slits scan adjacent and slightly overlapping wavelength regions. One complete scan with this deck covers the wavelength region 51 to 306 Å. For the other deck having a 300 line/mm grating, the wavelength scanning range is limited to four narrow regions of wavelength centered near the emission lines of FeXV at 284.15 Å, HeII at 303.78 Å, OV at 629.73 Å, and SiIII at 1206.52 Å. The HeII line is observed in third order at the wavelength position 911.34 Å. The wavelength range for each deck is established by limit switches that also reverse the scanning direction at each end of the wavelength range.

Table 1. Wavelength Regions Covered by Spectrometer

Channel <sup>a</sup>	Wavelength Range (Å) <sup>b</sup>	
1	51-100	
2	97-158	
3	156-228	
4	222-306	
5	277-291	FeXV 284.15
6	620-639	OV 629.73
7	901-923	HeII 303.78 (3rd order)
8	1194-1219	SiIII 1206.52

<sup>a</sup>Channels 1-4 on deck equipped with 1200 lines (FWHM = 0.25 Å);  
Channels 5-8 on deck with 300 lines/mm grating (FWHM = 2.5 Å).

<sup>b</sup>HeII 303.78 Å was observed in channel 7 in 3rd order at 911.34 Å.

A Galileo channel electron multiplier (CEM), an electron trap, and a pulse amplifier are mounted on each exit slit assembly, as shown in Figure 2. The radiation illuminated the inner side wall of the photocathode at an angle of incidence of 75° from the wall normal to obtain an increase in the photoelectric yield that occurs at wavelengths below about 300 Å (channels 1-4) as grazing

angles of illumination are approached.<sup>2,3</sup> In addition, the inner walls of the CEM's of channels 1 and 2 are coated with MgF<sub>2</sub> to enhance the quantum efficiencies<sup>4</sup> of these channels, which cover the wavelength range 51 to 158 Å, where the solar flux is low. The CEM's are operated as photon counters. Counts are accumulated in parallel for all channels at each position of the exit slit for 83 msec, the slit moved to its adjacent position, and the cycle repeated. The entrance and exit slits for channels 1-4 are 50 μ wide, and these matched slits produce a triangular line profile having a full width at half-maximum (FWHM) intensity of 0.25 Å. For channels 5-8, the widths of the entrance and exit slits are 50 μ and 125 μ, respectively. These line profiles are "flat topped" with a FWHM intensity of 2.5 Å. The entrance slit of each deck is 5 mm long, and the exit slits of all channels are 12 mm long. The time required to scan the complete wavelength range 51 to 306 Å, covered by channels 1-4, is 123 sec, and the time required to scan the limited wavelength regions of channels 5-8 is 4.5 sec. The individual lines that are centered in channels 5-8 (Table 1) were, therefore, scanned every 4.5 sec during the rocket flight, permitting the flux of these lines to be measured as a function of altitude.

### 3.2 Radiometric Calibration of the Spectrometer

The radiometric efficiency  $\epsilon(\lambda)$  in counts photon<sup>-1</sup> of the rocket spectrometer was determined in the laboratory by using an auxiliary monochromator to produce monochromatic emission lines and x-ray bands distributed in wavelength between 45 and 1216 Å. The efficiency  $\epsilon(\lambda)$  is determined from the ratio  $N(\lambda)/\phi(\lambda)$ , where  $N(\lambda)$  is the recorded counting rate of the spectrometer at wavelength  $\lambda$  when the grating is illuminated with a photon beam  $\phi(\lambda)$  of known rate. The photon rate  $\phi(\lambda)$  was determined by inserting either a gas-flow thin-window Geiger-Mueller (GM) counter or a tungsten-cathode photodiode into the photon beam between the entrance slit and grating of the spectrometer. The GM counter, operated with argon, was used as an absolute photon counter<sup>5</sup> to calibrate the spectrometer between 45 and 256 Å. This counter was similar in design to that used by Manson<sup>6</sup>

2. Rumsh, M. A., Lukirskii, A. P., and Shchemelev, V. N. (1960) Dokl. Akad. Nauk USSR 135:55 [English translation: Soviet Physics-Doklady 5:1231].
3. Heroux, L., Manson, J. E., Hinteregger, H. E., and McMahon, W. J. (1965) Photoelectric yields for oblique incidence of extreme ultraviolet radiation, J. Opt. Soc. Am. 55:103.
4. Lapson, L. B., and Timothy, J. G. (1976) Channel electron multipliers: detection efficiencies with opaque MgF<sub>2</sub> photocathodes at XUV wavelengths, Appl. Opt. 15:1218.
5. Ederer, D. L., and Tomboulian, D. H. (1964) The performance of a Geiger-Mueller counter in the 100-300 Å region, Appl. Opt. 3:1073.
6. Manson, J. E. (1972) Measurements of the solar spectrum between 30 and 128 Å, Solar Phys. 27:107.

as a detector in a rocket spectrometer to measure solar flux between 30 and 130 Å. The tungsten photodiode was used to determine  $\epsilon(\lambda)$  for the overlapping wavelength region 256 to 1216 Å. A National Bureau of Standards  $\text{Al}_2\text{O}_3$  photodiode was used as a transfer standard to calibrate the tungsten photodiode.

The auxiliary laboratory monochromator was equipped with an x-ray source to produce the K emission bands of C at 44 Å, B at 67 Å, and Be at 113 Å. This source was replaced with a hollow cathode discharge source to produce radiation at longer wavelengths. When the hollow cathode source is operated with a gas mixture of 90 percent neon and 10 percent helium, emission lines of NeIII and IV between about 135 to 258 Å are produced.<sup>7</sup> When the source is operated with other gases such as H, He, Ne, Ar, and Kr, several intense resonance series lines of these elements are produced that extend in wavelength from about 236 to 1236 Å.

### 3.3 The Solar Flux

The solar  $F_{10.7}$  cm radio emission was  $154.2 \times 10^{-22} \text{ Wm}^{-2} \text{ Hz}^{-1}$  at the time of the rocket flight. The axis of the spectrometer was pointed at the center of the sun with a Ball Research Corporation biaxial solar pointing control. The solar zenith angle was 25°. Radiation from the full solar disk was measured. One complete scan of the wavelength region 51 to 306 Å, measured with channels 1-4, was obtained between 170 km (rocket ascent) and 147 km (rocket descent). The peak altitude of the rocket was 178 km. For channels 5-8, approximately 33 scans were obtained as a function of altitude between 178 and 127 km.

Table 2 gives the integrated values of solar flux incident on the earth's atmosphere in 10-Å intervals between 1026 and 50 Å. The flux of the prominent spectral lines, also given in the table, are included in the integrated values of flux for the wavelength interval in which they fall. With the exception of the rocket measurements of the OV line at 629.73 Å and the wavelength region 50 to 306 Å, the fluxes given in Table 2 were obtained from the AE-E satellite spectrometer. The fluxes of the FeXV and HeII lines at 284.15 and 303.78 Å, respectively, measured in channels 5 and 7 of the rocket spectrometer agreed with the fluxes of those lines measured in channel 4 to within the estimated limits of error. The estimated errors for the fluxes given in Table 2 are ±30 percent.

The fluxes in Table 2 that were obtained from the rocket experiment were corrected for atmospheric absorption. These top of the atmosphere fluxes  $\phi_o(\lambda)$  in  $\text{ph cm}^{-2} \text{ s}^{-1}$  were obtained by correcting the flux  $\phi_h(\lambda)$  measured at altitude h for atmospheric absorption according to the equation

7. Manson, J. E. (1973) Light source and filters for use in the 130-280 Å region, Appl. Opt. 12:1394.

Table 2. Solar Flux for 14 August 1979, at 2020 UT

Wavelength, Å	Ion	Flux, $10^9 \text{ ph cm}^{-2} \text{ s}^{-1}$
1025.72	HI	10.7
1026-1020		10.9
1010.20	CII	0.146
1020-1010		0.407
1010-1000		0.218
999.55	NIII	0.673
1000-990		0.855
989.79	NIII	0.336
990-980		0.488
977.02	CIII	9.11
972.54	HI	1.85
980-970		11.1
970-960		0.106
960-950		0.088
949.74	HI	0.928
944.52	SVI	0.132
950-940		1.13
937.80	HI	0.558
933.38	SVI	0.200
930.75	HI	0.403
940-930		1.22
926.20	HI	0.342
923.15	HI	0.249
920.96	III	0.174
930-920		0.817
920-910		1.52
904.10	CII	0.201
910-900		4.42
900-890		3.29
890-880		2.56
880-870		1.99
870-860		1.45
860-850		1.21
850-840		0.938

Table 2. Solar Flux for 14 August 1979, at 2020 UT (Cont.)

Wavelength, Å	Ion	Flux, $10^9 \text{ ph cm}^{-2} \text{ s}^{-1}$
834.20	OII, OIII	1.07
840-830		1.80
830-820		0.568
820-810		0.442
810-800		0.344
790.15	OIV	0.101
800-790		1.06
787.71	OIV	0.463
786.47	SV	0.234
780.32	NeVIII	0.289
790-780		1.19
770.41	NeVIII	0.536
780-770		0.718
765.15	NIV	0.368
762.00	OV	0.065
761.13	OV	0.043
760.30	OV	0.173
770-760		0.775
760-750		0.302
750-740		0.100
740-730		0.059
730-720		0.046
718.50	OII	0.085
720-710		0.142
703.36	OIII	0.627
710-700		0.654
700-690		0.080
685.71	NIII	0.178
690-680		0.235
680-670		0.018
670-660		0.019
660-650		0.054
650-640		0.104
640-630		0.055

Table 2. Solar Flux for 14 August 1979, at 2020 UT (Cont.)

Wavelength, Å	Ion	Flux, $10^9 \text{ ph cm}^{-2} \text{ s}^{-1}$
629.73	OV	2.68
624.93	MgX	0.254
630-620		2.93
620-610		0.027
609.76	MgX	1.14
610-600		1.14
599.60	OIII	0.304
600-590		0.347
584.33	HeI	3.94
590-580		3.96
580-570		0.152
570-560		0.253
554.37	OIV	1.43
560-550		1.58
550-540		0.034
540-530		0.394
520.66	SiXII	0.329
530-520		0.450
520-510		0.071
510-500		0.339
499.37	SiXII	0.717
500-490		0.918
490-480		0.135
480-470		0.071
465.22	NeVII	0.559
470-460		0.600
460-450		0.020
450-440		0.00
440-430		0.313
430-420		0.00
417.24	FeXV	0.202
420-410		0.202

Table 2. Solar Flux for 14 August 1979, at 2020 UT (Cont.)

Wavelength, Å	Ion	Flux, $10^9 \text{ ph cm}^{-2} \text{ s}^{-1}$
410-400		0.304
400-390		0.026
390-380		0.00
380-370		0.00
368.07	MgIX	1.19
360.80	FeXVI	0.980
370-360		2.43
360-350		0.331
350-340		1.05
335.41	FeXVI	1.90
340-330		1.90
330-320		0.289
320-310		0.994
303.78	HeII	8.70
303.31	SiXI	1.79
310-300		10.49
296.19	SiIX	0.116
292.83	SiIX	0.102
300-290		0.370
289.17	FeXIV	0.125
284.15	FeXV	2.30
290-280		2.71
277.26	SiX	0.137
274.22	FeXIV	0.600
271.995	SX	0.146
270.51	FeXIV	0.280
280-270		1.49
264.80	FeXIV	0.462
264.24	SX	0.154
262.99	FeXVI	0.159
261.06	SiX	0.170
270-260		1.02
259.52	SX	0.086
258.35	SiX	0.272
257.3	FeXIV, SX	0.345
256.6	FeXV, SXIII, SiX, HeII	0.627
253.78	SiX	0.066
252.0	FeXIV, FeXIII	0.297

Table 2. Solar Flux for 14 August 1979, at 2020 UT (Cont.)

Wavelength, Å	Ion	Flux, $10^9 \text{ ph cm}^{-2} \text{ s}^{-1}$
251.06	FeXVI	0.060
260-250		1.82
249.18	NiXVII	0.070
246.21	FeXIII	0.128
244.91	FeIX	0.094
243.78	FeXV	0.131
243.03	HeII	0.126
241.74	FeIX	0.145
240.71	FeXIII	0.094
250-240		0.900
237.2	HeII, SiXIV, FeXII	0.056
234.4	HeII, FeXIV, SXII	0.072
240-230		0.342
227.01	SiIX	0.085
230-220		0.780
211.32	FeXIV	0.290
220-210		0.605
203.81	FeXIII	0.110
210-200		0.697
195.13	FeXII	0.374
193.52	FeXII	0.229
200-190		1.16
188.31	FeXI	0.281
184.53	FeX	0.080
180.41	FeXI	0.419
190-180		1.07
177.24	FeX	0.298
174.58	FeX	0.492
171.08	FeIX	0.494
180-170		1.53
170-160		0.274
157.73	NiXIII	0.048
154.18	NiXII	0.034
152.15	NiXII	0.065
150.10	OVI	0.019
160-150		0.210
148.40	NiXI	0.071
150-140		0.121
140-130		0.023
130-120		0.034

Table 2. Solar Flux for 14 August 1979, at 2020 UT (Cont.)

Wavelength, Å	Ion	Flux, $10^9 \text{ ph cm}^{-2} \text{ s}^{-1}$
120-110		0.047
110-100		0.057
98.2	NeVIII	0.012
96.12	FeX	0.015
95.35	FeX	0.009
94.01	FeX	0.015
100-90		0.180
88.09	NeVIII	0.010
86.8	FeXI, NiX	0.014
82.8	FeXII	0.018
90-80		0.175
75.89	FeXIII	0.018
73.47	FeXV	0.017
80-70		0.218
69.70	SiVII, SiVIII	0.031
66.37	FeXVI	0.019
66.26	FeXVI	0.019
70-60		0.236
60-50		0.193

$$\phi_h(\lambda) = \phi_o(\lambda) e^{-\tau}, \quad (1)$$

where the optical depth  $\tau$  is given by

$$\tau = \sum_j \sigma_j(\lambda) \int_h^\infty n_j(h) dh \sec x. \quad (2)$$

The subscript  $j$  refers to the atmospheric constituents,  $\sigma_j(\text{cm}^2)$  is the absorption cross section,  $n_j(\text{cm}^{-3})$  is the density of constituent  $j$  as a function of altitude, and  $x$  is the solar zenith angle relative to the vertical direction. The exponential was evaluated at the altitude at which the radiation of wavelength  $\lambda$  was measured during the rocket flight. The densities of the constituents  $N_2$ ,  $O_2$ , and  $O$  were obtained by using the model atmosphere of Jacchia,<sup>8</sup> and the absorption cross

---

8. Jacchia, L.G. (1977) Smithsonian Astrophysical Observatory, Special Report 375.

sections were those given by Huffman.<sup>9</sup> Slight modifications in the cross sections of Huffman were applied, where the modifications were based on solar UV absorption measurements made on the Atmosphere Explorer satellite by Hinteregger and on values of cross sections given by Kirby et al.<sup>10</sup>

The incident flux  $\phi_o(\lambda)$  is obtained from the equation

$$\phi_o(\lambda) = \phi_h(\lambda) e^T . \quad (3)$$

The correction factor  $e^T$  depends on the wavelength and the altitude at which the wavelength is scanned during flight. This factor covered a wide range for the flight of 14 August 1979. For the emission line of HeII at 304 Å measured near 150 km,  $e^T$  was approximately 6; for the line of HeII at 256 Å measured near 178 km,  $e^T$  was 1.8. Because the cross sections decrease rapidly with decreasing wavelength, the values of  $e^T$  were considerably smaller than the above values for wavelengths below 180 Å. For example, the values of  $e^T$  for the wavelength intervals near 115 Å and 68 Å measured near the peak altitude of 178 km were 1.13 and 1.03, respectively.

The magnitude of absorption of solar radiation near 304 Å is illustrated in Figure 3, where the flux of the unresolved lines of HeII at 303.78 Å and SiXI at 303.31 Å is plotted as a function of altitude. These data were obtained from channel 7 (see Table 1), which has a low spectral resolution (FWHM = 2.5 Å). Approximately 83 percent of the flux of the unresolved lines given in Figure 3 originates from the HeII 303.78 Å line, as can be seen from the data given in Table 2, which was obtained from channel 4 in which the two emission lines of HeII and SiXI are clearly resolved.

#### 4. ELECTRON SPECTROMETER

##### 4.1 Experimental

Measurements of the differential energy distribution and flux of the thermospheric photoelectrons were made with the 127° cylindrical electrostatic deflection analyzer illustrated in Figure 4. The instrument was essentially identical to that described previously McMahon and Heroux,<sup>11</sup> but it had aperture

9. Huffman, R. E. (1969) Absorption cross sections of atmospheric gases for use in aeronomy, Can. J. Chem. 47:1823.
10. Kirby, K., Constantinides, E. R., Babeau, S., Oppenheimer, M., and Victor, G. A. (1978) Harvard-Smithsonian Center for Astrophysics, Preprint Series No. 1018, submitted to Atomic Data and Nuclear Tables.
11. McMahon, W. J., and Heroux, L. (1978) Rocket measurement of thermospheric photoelectron energy spectra, J. Geophys. Res. 83:1390.

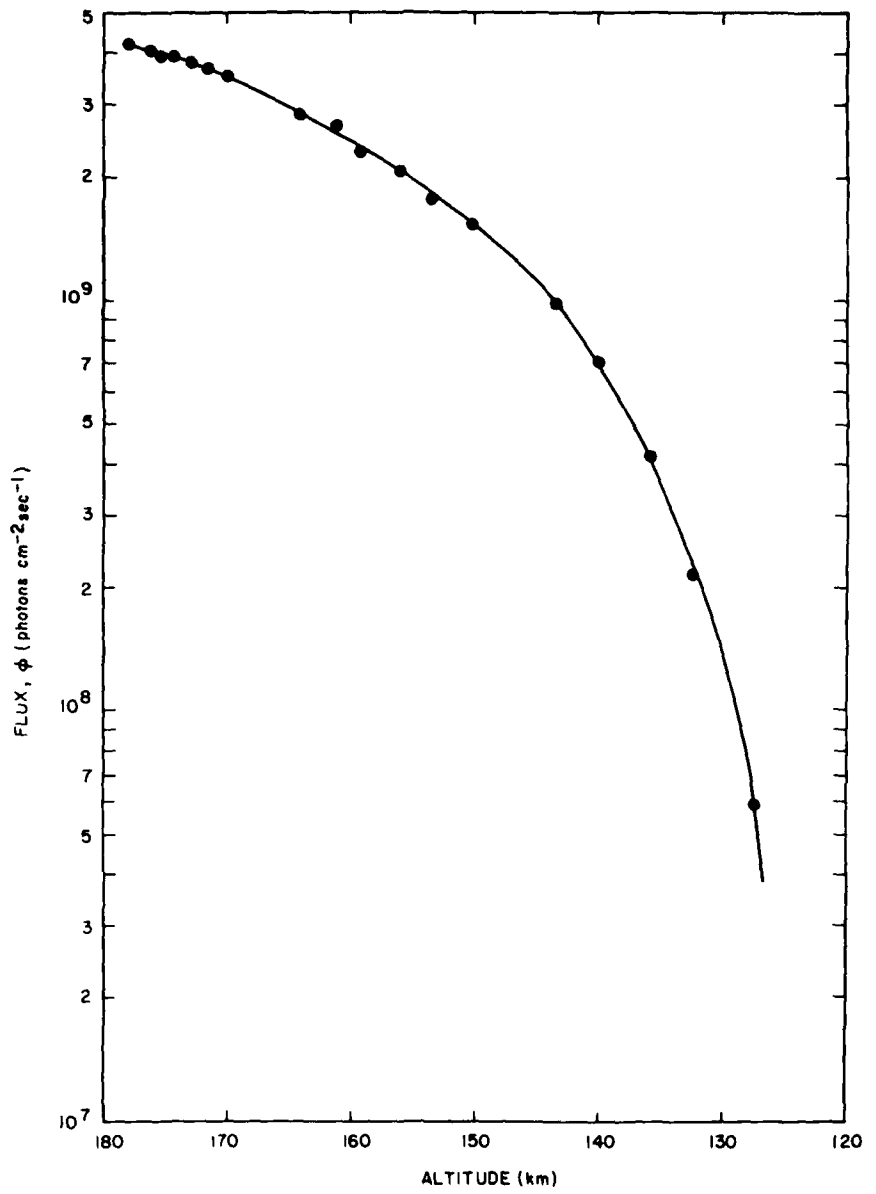


Figure 3. The Absorption of the Unresolved Solar Emission Lines of HeII and SiXI at 303.78 and 303.31 Å, Respectively, as a Function of Altitude. Approximately 83 percent of the flux of the unresolved lines originates from the HeII line

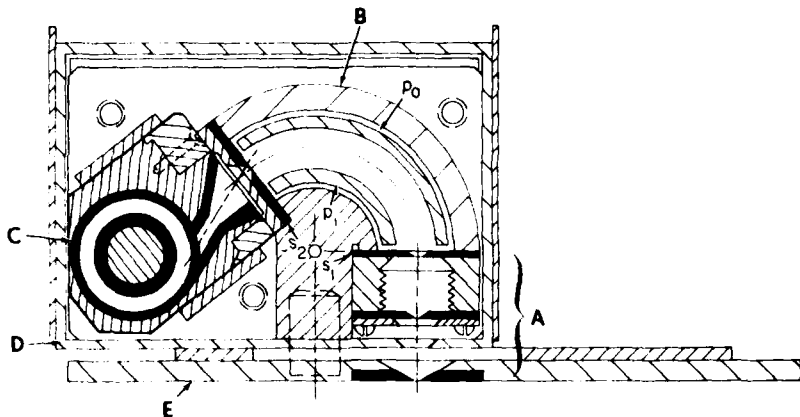


Figure 4. Cross Section of the Electron Energy Analyzer. A indicates the collimating aperture assembly, B the 127° deflection analyzer assembly, C the detector assembly, D the magnetic shield, and E the aperture field plate.  $S_1$  indicates the analyzer entrance slit and field stop and  $S_2$  the exit slit.  $p_0$  and  $p_i$  indicate the outer and inner deflection plates

modifications to obtain improved energy resolution. Energy scans were made in 64-step sequences with the first 40 steps dedicated to the energy region between 0.89 and 4.2 eV (nominal). The remaining 24 steps scanned the nominal energy region between 13 and 32 eV. Stepping increments were limited to the equivalent energy bandpass increments to minimize data dropout between steps. This consequently limited continuous range coverage and is the reason for dividing the scan sequence into the two assigned regions where the most significant energy structure was anticipated.

The mounting of the instrument maintained the entrance aperture of the analyzer in a sun-shaded position throughout the flight (see Figure 1) to eliminate signal contamination by locally generated photoelectrons. An adjustable mounting assembly allowed preflight alignment of this aperture axis so that it was held essentially parallel to the geomagnetic vector during the data acquisition period. This alignment is critical for the measurement of low energy electrons, because it eliminates the effects of geomagnetic shadowing; additionally, it allows a valid correction to be made for vehicle skin charge  $V_S$ , which can induce substantial data degradation for energies below about 10 eV. Since it is generally accepted that the angular distribution of thermospheric photoelectrons is isotropic below about 250 km, pitch angle sampling was not necessary.

The analyzer was calibrated at the Rice University particle detector calibration facility. The instrument parameters that were determined are: geometric

factor,  $5.7 \times 10^{-4} \text{ cm}^2 \text{ sr}$ ; solid agreement angle,  $7.5^\circ \times 9.5^\circ$ ; energy resolution, 7 percent; and instrument constant, the ratio of analyzer voltage to electron energy, 1.27. The accurate determination of these instrument parameters is critical to the reduction of flight data to obtain valid energy measurements, particularly those related to absolute flux values.

#### 4.2 Results

Data were corrected for an assigned  $V_s$  value of -1.5 V. This was determined by inspection of the raw spectra in the energy region between 20 and 30 eV that contains structure due to the production of primary photoelectrons of known energy originating from the photoionization of O and N<sub>2</sub> by the solar HeII emission line at 303.78 Å. This value of  $V_s$  has an estimated accuracy to within  $\pm 0.5$  V. It is less precise than expected because of unanticipated broadening of these structural features observed during the flight. Figure 5 illustrates the observed structure in this energy region as a function of altitude. Each curve represents the mean of several adjacent scans that were summed to obtain better statistics. This procedure determined the altitude resolution so that the range of altitudes about the average altitude plotted is less than  $\pm 2$  km, except for the lowest altitude curve where the altitude range is  $\pm 3$  km. The absolute flux levels shown are a factor of approximately 2 lower than those measured by Doering et al,<sup>12</sup> but are more nearly in agreement with those predicted by theory by Victor et al<sup>13</sup> and Jasperse.<sup>14</sup>

The structure in the 20 to 28 eV region as a function of altitude appears broadened when compared with that observed in the earlier flight,<sup>11</sup> although the resolution of the present analyzer is a factor of 2 higher than that of the analyzer previously used. This is illustrated particularly by the structure observed at the lower altitude limits. As expected, the structural features diminish with decreasing altitude, and, in the present case, are not observable below about 140 km. In the earlier measurements this structure was clearly observable down to nearly 120 km. This difference can be explained by the high values of atmospheric density for 14 August 1979 that resulted in strong atmospheric absorption of the HeII 303.78 Å line. As discussed in Section 3.3, this line was attenuated by a

---

12. Doering, J. P., Peterson, W. K., Bostrom, C. O., and Potemra, T. A. (1976) High resolution daytime photoelectron energy spectra from AE-E, Geophys. Res. Lett. 3:129.
13. Victor, G. A., Kirby-Docken, K., and Dalgarno, A. (1976) Calculations of the equilibrium photoelectron flux in the thermosphere, Planet. Space Sci. 24:679.
14. Jasperse, J. R. (1977) Electron distribution functions and ion concentrations in the earth's lower ionosphere from Boltzmann-Fokker-Planck theory, Planet. Space Sci. 25:743.

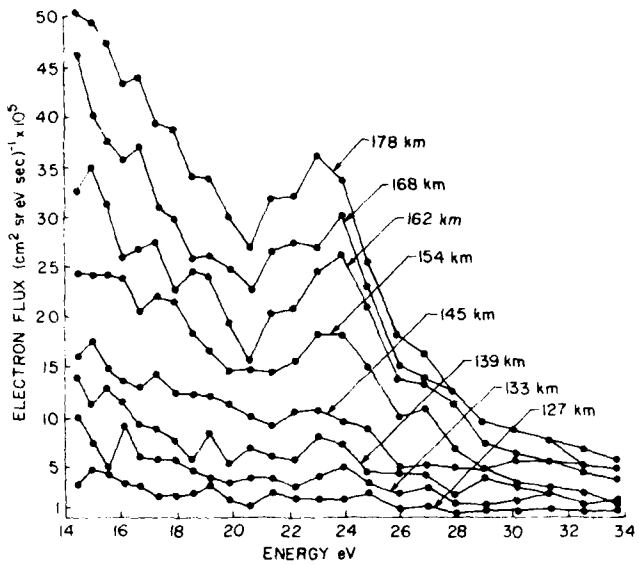


Figure 5. The Photoelectron Energy Distribution Between 14 and 34 eV

factor of 6 at an altitude of 150 km. The absorption of this line over the altitude range 178 to 127 km is also given in Figure 3. The altitude range over which the structure could be observed in the present experiment was also limited by the peak height of 178 km for the rocket in contrast to the peak height of 230 km for the previous rocket flight.

Figure 6 shows the lower energy segment of the observed spectra between 2.4 and 5.7 eV after correction for  $V_S = -1.5$  V. These curves were obtained from a greater number of data points (closer energy increments) than those of Figure 5. Since there was no consistently observed substructure, these data are presented as smooth curves. The characteristic valley-like structure in this region, attributed to resonant-vibrational excitation of  $N_2$ , also appears to be reduced in prominence from that observed earlier, although the significance of that comparison here must be treated cautiously because the possibility of quantitative error is much greater in the region below 10 eV. It is in this region that the accurate assessment of the skin-charge value  $V_S$  becomes critical in correcting for signal changes. However, valid relative comparisons between adjacent spectra obtained in the same experiment can be made. As shown in Figure 6 the valley-like structure is clearly present and also decreases in prominence as the altitude decreases, disappearing below about 130 km. This behavior is consistent

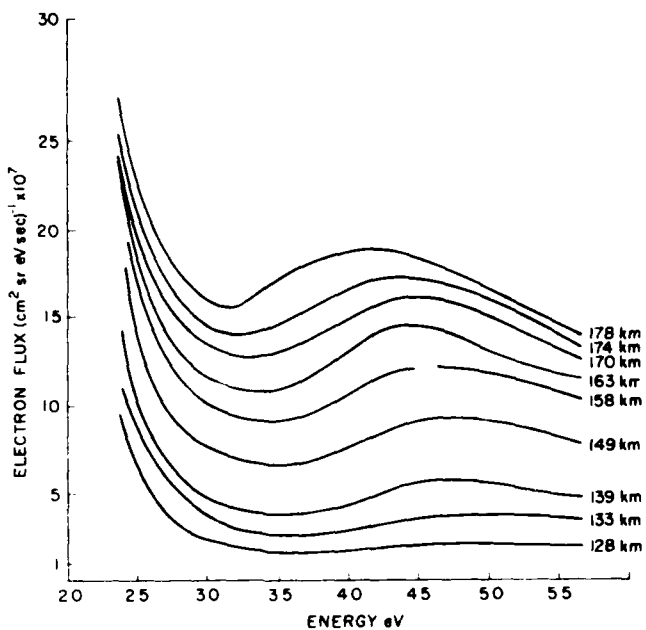


Figure 6. The Photoelectron Energy Distribution Between 2.4 and 5.7 eV

with the earlier observations, but is in conflict with current theory which predicts increased prominence of this structural feature as the altitude decreases below about 200 km, approaching a limit at 100 km.

### 5. NITROGEN SECOND POSITIVE AIRGLOW MEASUREMENTS

This section describes the  $N_2$  second positive photometer and analyzes the data in terms of both column and volume emission rates. The photometer calibration procedure is described in detail.

#### 5.1 The Dayglow Photometer

The dayglow photometer consisted of a three-stage baffle system, lenses, four-position filter wheel, and a single photomultiplier tube with its associated high-voltage power supply, pulse-counting amplifier, and discriminator. The optical layout is shown in Figure 7. The three-stage baffle system was designed to allow observations of airglow radiation to within  $30^\circ$  of the sun. The baffles

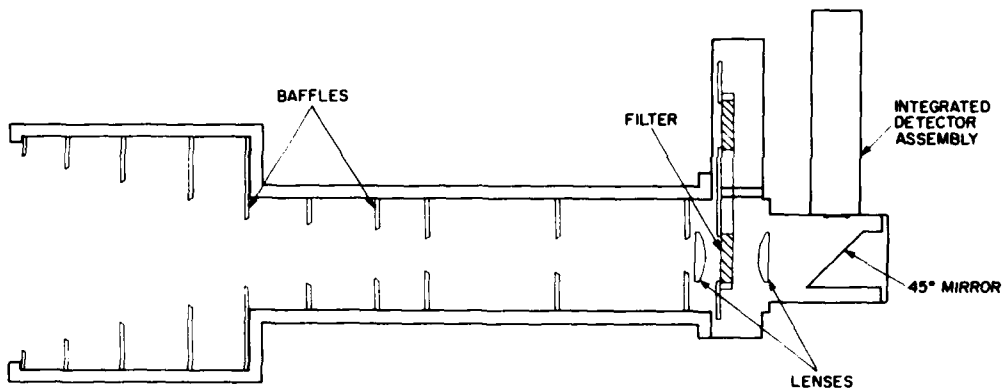


Figure 7. Schematic Diagram of the Dayglow Photometer

were arranged as described by Smith<sup>15</sup> so that no surface or edge could "see" both the collimating lens and any surface or edge that was illuminated directly by the sun. With this arrangement sunlight must be scattered from three successive edges to be detected. The scattering from each edge was minimized by coating the baffles and edges with Martin Marietta Optical Black Coating.

The diameter of both the aperture and field stop was 1.5 cm. They were spaced 135 cm apart. This produces a vignetted field with a half-angle of 6° and throughput ( $A\Omega$ ) of  $0.017 \text{ cm}^2 \text{ sr}$ . The collimating lens reduced the divergence of the rays going through the filter to 3°. The condensing lens imaged all the rays onto the detector, an EMR photomultiplier 5101N-03-13, which was incorporated into a Spa Com Integrated Detector System, Model SE 325. Counts from the discriminator were collected in counters, read, and shifted every 100 msec.

Three individual interference filters and an opaque mask were mounted in the filter wheel that was driven by a Geneva mechanism. The filter wheel made one complete revolution every 3.2 sec. Each filter was in position for 600 msec. Moving from one filter to the next required 200 msec. Two filters were centered at 3371 Å to measure the in-band radiation, one at 3260 Å to measure the background continuum, and an opaque section to monitor the dark count. The output with the different filters in place are designated as channels.

### 5.2 Calibration of the Photometer

Photometric calibration of the three channels was performed to measure the intensity of the nitrogen second positive band system. Because different

---

15. Smith, W.J. (1960) Modern Optical Engineering, McGraw-Hill Book Co., New York.

investigators use different calibration procedures and terminology, the calibration procedure used in this work will be described in detail.

The output of the photometer is given by the equation

$$S = (10^6/4\pi) \int_{\lambda} R_{\lambda}(\lambda) A \Omega Q(\lambda) T(\lambda) d\lambda , \quad (4)$$

where  $S$  is the signal in counts  $\text{sec}^{-1}$ ,  $R_{\lambda}(\lambda)$  is the spectral brightness of the source in rayleighs  $\text{\AA}^{-1}$ ,  $A$  is the area of the aperture in  $\text{cm}^2$ ,  $\Omega$  is the solid angle of the field in sr,  $Q(\lambda)$  is the quantum efficiency of the detector,  $T(\lambda)$  is the transmission of the system, and  $\lambda$  is the wavelength in  $\text{\AA}$  that extends over the wavelength range of the sensitivity of the instrument. It is convenient to combine the constants and instrumental factors to give

$$S = \int R_{\lambda}(\lambda) C(\lambda) d\lambda , \quad (5)$$

where  $C(\lambda) = (10^6/4\pi) A \Omega Q(\lambda) T(\lambda)$  and has units of counts  $\text{R}^{-1} \text{ sec}^{-1}$ .

The calibration function,  $C(\lambda)$ , may be separated into a constant factor,  $C_o$ , and a wavelength dependent parameter,  $\eta(\lambda)$ , chosen such that  $C(\lambda)$  equals  $C_o$  at  $\lambda_o$ , the wavelength of peak sensitivity. Thus  $\eta(\lambda)$  becomes the relative instrumental response.

Substituting  $C_o \eta(\lambda)$  into Eq. (5) gives

$$S = C_o \int R_{\lambda}(\lambda) \eta(\lambda) d\lambda . \quad (6)$$

### 5.2.1 THE RELATIVE INSTRUMENTAL RESPONSE, $\eta(\lambda)$

The relative instrumental response is determined by means of a continuous source followed by a monochromator arranged to illuminate a screen large enough to fill the field-of-view of the photometer as shown in Figure 8. The spectral brightness of the screen at wavelength  $\lambda'$  is given by

$$R_{\lambda, M}(\lambda, \lambda') = C_{\lambda, M}(\lambda) m(\lambda, \lambda') , \quad (7)$$

where  $\lambda$  is the monochromator wavelength setting,  $m(\lambda, \lambda')$  is its relative response, and  $C_{\lambda, M}(\lambda)$  is a factor that depends only on the wavelength variation of the monochromator peak transmission and the monochromator illuminator brightness.

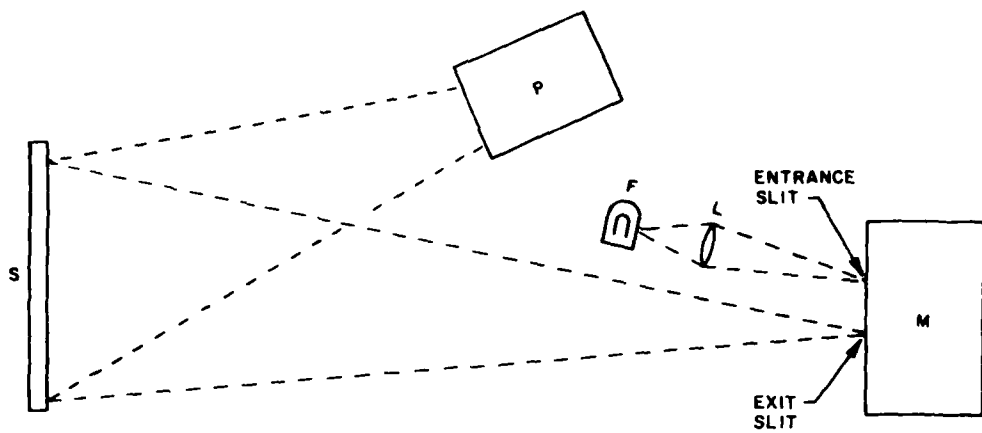


Figure 8. Schematic Arrangement for Determining the Instrument Response Function. P, photometer; S, screen; M, monochromator; L, lens; F, filament

Substituting Eq. (5) into Eq. (6) gives the output from the photometer as

$$S(\lambda) = C_o \int C_{\lambda, M}(\lambda) m(\lambda, \lambda') \eta(\lambda) d\lambda' \quad (8)$$

which is approximately equal to  $C_o C_{\lambda, M}(\lambda) \eta(\lambda)$  if the monochromator response is sufficiently narrow so that  $\eta(\lambda')$  may be taken to have a constant value  $\eta(\lambda)$  over the region where  $m(\lambda, \lambda')$  differs significantly from zero.

As mentioned previously, the variation in  $C_{\lambda, M}(\lambda)$  results from variations in the monochromator peak transmission and illuminator brightness. It should be nearly constant over the narrow band pass of the photometer, in which case its response function,  $\eta(\lambda)$ , can be determined directly by plotting the signal as a function of the wavelength setting of the monochromator.

The relative spectral response of the three filters is shown in Figures 9, 10, and 11. The two in-band filters are designated 0 and 3, while the background filter is designated 2.

The data points were fitted to a curve of the form  $e^{-a|\lambda - \lambda_0|^b}$  where a, b, and  $\lambda_0$  as well as  $W_{eq}$ , the equivalent width, are given in Table 3. The equivalent width is defined as  $\int \eta(\lambda) d\lambda$ .

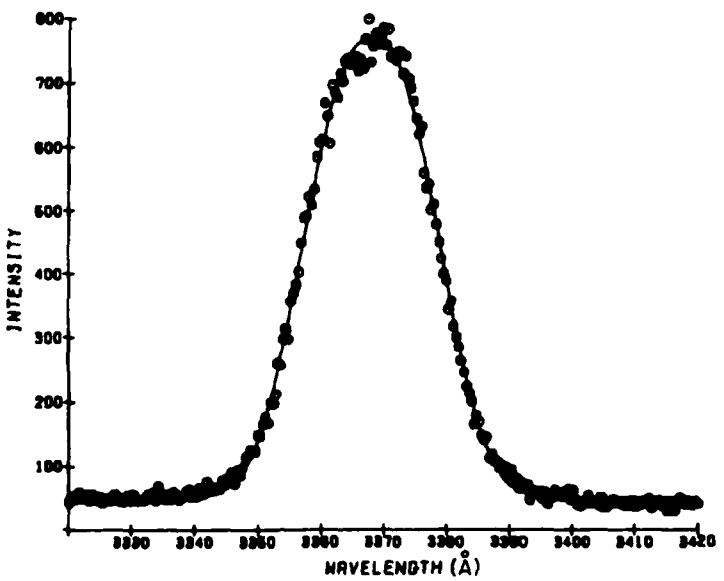


Figure 9. Relative Spectral Response of Channel 0. The solid line indicates the fit using the parameters given in Table 1

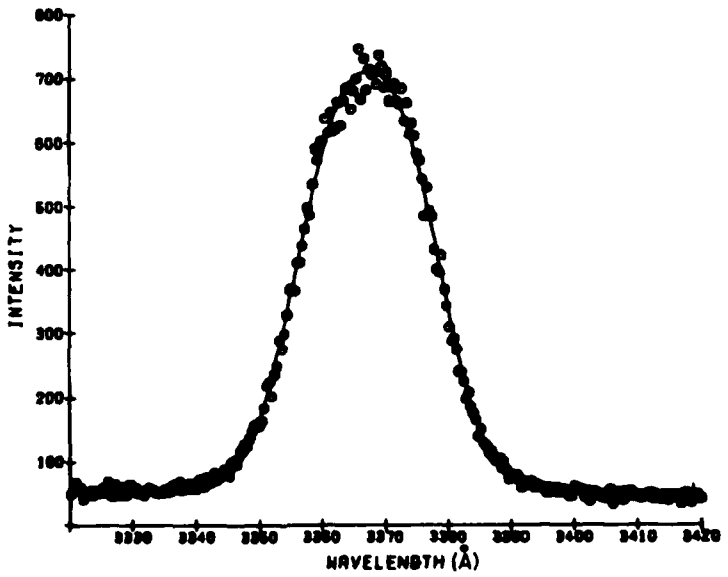


Figure 10. Relative Spectral Response of Channel 3. The solid line indicates the fit using the parameters given in Table 1

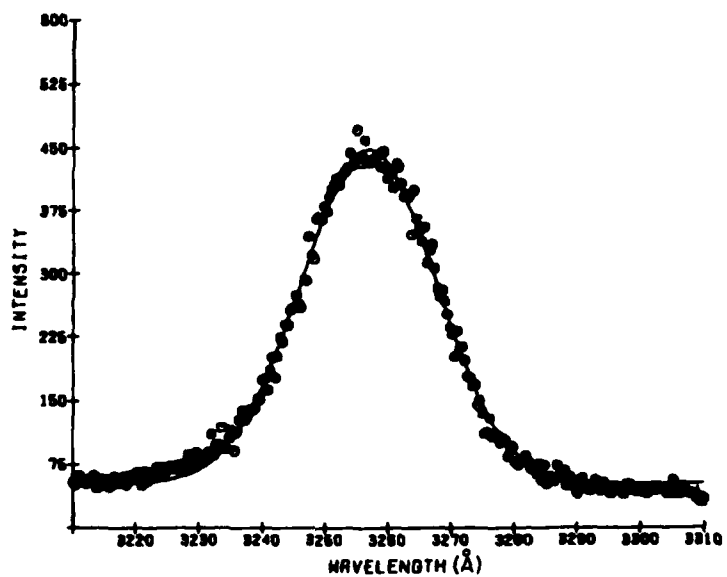


Figure 11. Relative Spectral Response of Channel 2. The solid line indicates the fit using the parameters given in Table 1

Table 3. Channel Parameters (see text)

Channel Number	$\lambda_o$ (Å)	a	b	$W_{eq}$ (Å)
0	3368.0	0.00141	1.965	24.0
3	3367.2	0.00158	2.467	24.2
2	3256.9	0.00438	2.525	26.8

### 5.2.2 THE CALIBRATION FACTOR, $C_o$

The absolute response was determined by viewing a screen that has been coated with a standard reflectance coating and is illuminated by a calibrated standard lamp. The reflectance coating is composed of highly purified barium sulfate. It is available commercially as Eastman White Reflectance Coating. This coating is completely non-self radiating and is characterized by high

stability and a nearly perfect reflecting surface; it has an absolute reflectance of nearly 98 percent in the spectral region used here.<sup>16</sup>

The standard lamp is provided with absolute calibration of spectral irradiance,  $I_{\lambda}(\lambda)$ , in units of  $\text{W cm}^{-2} \text{nm}^{-1}$  measured at 0.5 m by EG&G. It is directly traceable to the National Bureau of Standards. The lamp is enclosed in an NBS type holder that is in turn fitted with a light-tight filter holder that is used to hold neutral density filters. Both the lamp and filter holders were constructed in such a manner as to reflect a negligible amount of radiant flux in the direction of the screen. A black shield placed between the source holder and the screen was used to further control stray light.

The spectral irradiance of the lamp at a distance of 50 cm is shown in Figure 12. The absolute accuracy of the lamp in this region is given as 2 percent. The distance from the lamp to the screen was 6.35 m; the inverse-square law is used to calculate the spectral irradiance falling on the screen at this distance.

The conversion of the spectral irradiance at the screen in units of  $\text{W cm}^{-2} \text{nm}^{-1}$  to the spectral brightness of the screen in units of rayleighs  $\text{\AA}^{-1}$  is given by

$$R_{\lambda}(\lambda) = 2.014 \times 10^8 \lambda I_{\lambda} r(\lambda) \quad (9)$$

where  $r(\lambda)$  is the absolute reflectance of the coating;  $\lambda$  is given in  $\text{\AA}$ .

Once the spectral brightness of the screen is determined, the calibration factor may be calculated by rearranging Eq. (6); thus,

$$C_o = S / \int R_{\lambda}(\lambda) \eta(\lambda) d\lambda \quad . \quad (10)$$

If the bandwidth of the photometer is narrow relative to the wavelength variation in the output of the standard lamp, as it is here, the integral in Eq. (10) may reduce to  $R_{\lambda_o}(\lambda_o) W_{eq}$  where  $R_{\lambda_o}(\lambda_o)$  is the spectral brightness of the screen at  $\lambda_o$ , the wavelength of peak sensitivity.

A summary of the characteristics of each of the photometer channels is given in Table 4.

To use the photometer to determine the total emission of an airglow or auroral feature, it is necessary to know the spectral distribution of the feature and the contribution to the signal due to a background continuum or to light scattered into the instrument from sources outside its field-of-view. It is convenient to express this by writing the photometer equation as the sum of two terms,

16. Grum, F., and Luckey, G. W. (1968) Optical sphere paint and a working standard of reflectance, Appl. Opt. 7:2289.

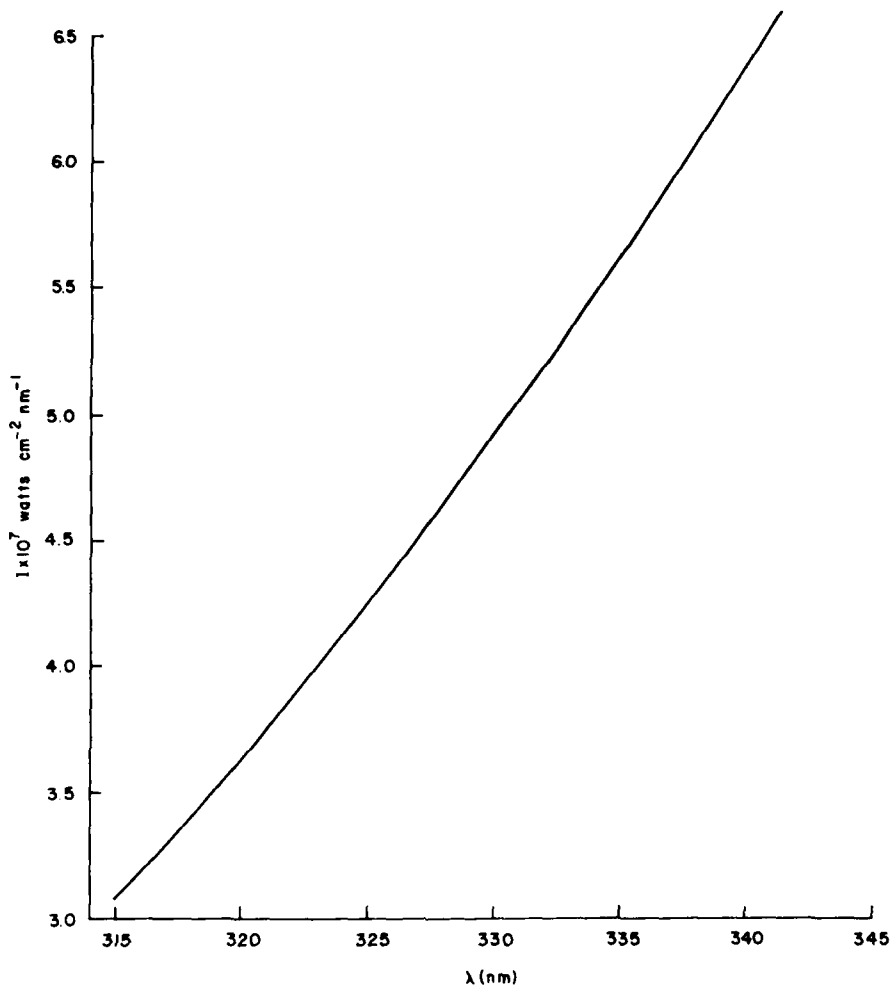


Figure 12. The Spectral Irradiance of the Calibrated Standard Lamp, FEL F056F, at 50 cm

$$S = C_o R_{\text{band}} \int \beta_\lambda(\lambda) \eta(\lambda) d\lambda + C_o \int R_\lambda(\lambda)_{\text{background}} \eta(\lambda) d\lambda , \quad (11)$$

where the first term represents the contribution due to the emission feature, and the second term the contribution due to the background continuum or to light scattered into the instrument. Here  $R_{\text{band}}$  represents the total number of rayleighs emitted in the vibration-rotation band, and  $\beta_\lambda(\lambda)$  the spectral distribution of

intensity within the band. The integral  $\int \beta_\lambda(\lambda) \eta(\lambda) d\lambda$  is known as the relative band response. It is the response of the photometer to the band relative to its response to a line emitted at  $\lambda_o$ . The spectral distribution of intensity  $\beta_\lambda(\lambda)$  is determined by knowledge of the emitting species and the mechanism of excitation.

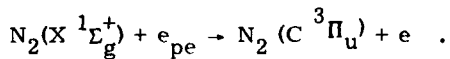
The contribution of the second term to the total signal is made by observations at a wavelength at which there is no contribution from the emission feature.

Table 4. Characteristics of Each of the Photometer Channels

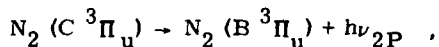
Channel Number	0	3	2
$\lambda_o$	3368.0	3367.2	3256.9
$W_{eq} (\text{\AA})$	24.0	24.2	26.8
$C_o W_{eq} (\text{counts sec}^{-1}/\text{RA}^{-1})$	774	789	736
$C_o (\text{counts sec}^{-1}/R)$	32.3	32.5	27.5

### 5.3 Mechanism of N<sub>2</sub> Second Positive Dayglow

Because the transition from the ground state to the excited state that gives rise to the N<sub>2</sub> second positive emission is optically forbidden, the excitation is believed to be caused entirely by fast photoelectrons,<sup>17</sup>



The subsequent decay to the B state,



is optically allowed and so occurs rapidly with no collisional quenching of the upper state.

---

17. Doering, J.P., Fastie, W.G., and Feldman, P.D. (1970) Photoelectron excitation of N<sub>2</sub> in the day airglow, J. Geophys. Res. 75:4787.

### 5.3.1 THE POSITION OF THE ROTATIONAL LINES

The position of the individual lines in the 0, 0 band have been given by Coster, et al.<sup>18</sup> The value of  $\nu_{0,0}$  is given by Huber and Herzberg<sup>19</sup> as  $29671.0 \text{ cm}^{-1}$ . The rotational constant,  $B_e$ , for the three states of importance in determining the band profile are shown in Table 5. The synthetic spectrum includes multiplet splitting, but neglects  $\Lambda$ -type doubling. Hund's case a applies, that is, the electronic motion is very strongly coupled to the line joining the nuclei, but only negligibly coupled to the nuclear rotation.

Table 5. Rotational Constants,  $B_e$ , for the X, B, and C States of Nitrogen (from Huber and Herzberg<sup>19</sup>)

State	$B_e$
X $^1\Sigma_g^+$	1.99824
B $^3\Pi_g$	1.63745
C $^3\Pi_u$	1.82473

The rotational terms are given by Herzberg<sup>20</sup> as  $F_\Omega(J) = B[J(J + 1) - \Omega^2]$ , where  $J$  and  $\Omega$  are integers such that  $J \geq \Omega$  and  $\Omega = 0, 1$ , or  $2$ . The positions of the lines are:

$$R_\Omega(J'') = F'_\Omega(J'' + 1) - F''_\Omega(J'') ; J'' = 0, 1, 2, \dots ,$$

$$Q_\Omega(J'') = F'_\Omega(J'') - F''_\Omega(J'') ; J'' = 1, 2, 3, \dots ,$$

$$P_\Omega(J'') = F'_\Omega(J'' - 1) - F''_\Omega(J'') ; J'' = 1, 2, 3, \dots .$$

The singly primed terms indicate the upper (C) state, and the doubly primed terms indicate the lower (B) state.

---

- 18. Coster, D., Brons, F., and Van der Ziel, A. (1933) Die sogenannte zweite positive gruppe des stickstoffspektrums, *Z. Physik*. 84:304.
- 19. Huber, K. P., and Herzberg, G. (1979) *Molecular Spectra and Molecular Structure, IV. Constants of Diatomic Molecules*, Van Nostrand Reinhold Co., New York.
- 20. Herzberg, G. (1950) *Spectra of Diatomic Molecules*, Second Edition, D. Van Nostrand Co., Inc., New York.

The positions as given in terms of wavenumbers in vacuo were converted to the positions in terms of wavelength in air by the expression

$$\lambda_{\text{air}} (\text{\AA}) = (1/n) 10^8 / \nu (\text{cm}^{-1}) , \quad (12)$$

where n is given by Edlen<sup>21</sup> as

$$n = 1 + 6432.8 \times 10^{-8} + \frac{2949810}{146 \times 10^8 - \nu^2} + \frac{25540}{41 \times 10^8 - \nu^2} . \quad (13)$$

### 5.3.2 THE RELATIVE INTENSITY OF THE ROTATIONAL LINES

The relative intensity of the lines is given by the product of the line strengths and the Boltzman factor. The value of the line strengths for Hund's case a are shown in Table 6.

Table 6. Line Strengths for Hund's Case a (Kovacs<sup>22</sup>)

Branch	Line Strength
P(J)	$\frac{J^2 - \Omega^2}{J}$
Q(J)	$\frac{\Omega^2(2J + 1)}{J(J + 1)}$
R(J)	$\frac{(J + 1)^2 - \Omega^2}{(J + 1)}$

The Boltzman factor is given by  $\exp [-B_e(X^1\Sigma_g^+) J' (J' + 1) hc/kT]$ , where the rotational constant is that of the ground state, and the temperature is that of the neutral atmosphere in degrees Kelvin. The rotational constant of the ground state molecule is used because no significant change in the angular momentum of the system is produced as the molecule is excited by photoelectron impact. Thus the distribution of molecules over the different rotational levels in the upper

---

- 21. Edlen, B. (1953) The dispersion of standard air, J. Opt. Soc. Am. **43**:339.
- 22. Kovacs, I. (1969) Rotational Structure in the Spectra of Diatomic Molecules, American Elsevier Publishing Co., Inc., New York.

electronic state is practically the same as in the ground state where, due to numerous molecular collisions, the distribution corresponds to thermal equilibrium of the neutral atmosphere.

The spectral distribution of intensity,  $\beta_\lambda(\lambda)$ , is shown in Figures 13a-h for atmospheric temperatures ranging from 200°K to 900°K in steps of 100°.

The relative band response,  $\int \beta_\lambda(\lambda)\eta(\lambda) d\lambda$ , of photometer channels 0 and 3 is shown in Figure 14 for temperatures ranging from 200° to 1000°K.

#### 5.4 Flight Data

The photometer and its door were driven out to make observations of airglow, as shown in Figure 1. In this configuration the optical axis of the photometer was 30° from the rocket axis. The rocket attitude was particularly stable, as indicated in Figures 15 and 16 which show the actual pointing direction of the photometer in elevation and azimuth.

Data obtained between 110 km and 160 km on the upleg portions of the flight exhibited highly irregular count rates and were discarded. Postflight analysis indicated that this was caused by light leaking past the filters, causing the sporadically high count rates. The instrument worked satisfactorily throughout the rest of the flight. The downleg data is presented here.

The data in counts per 100 msec frame are shown in Figures 17, 18, and 19 for filters 0, 3, and 2. Filters 0 and 3 represent inband 3371 Å observations, and filter 2 represents background at 3260 Å. The dark count in 10-frame sums is shown in Figure 20. The dark count was constant at about 24 counts per second throughout the flight.

The smooth line through the data in Figures 17, 18, and 19 was generated by two successive smoothing operations. The count rate was first determined in 1-km intervals by fitting a cubic that extended 8 km on each side of the altitude being fitted. This was further smoothed by fitting a quadratic that extended 10.5 km on each side. This technique resulted in a curve that was quite smooth and in which the residuals were uniformly distributed.

The contributions of second positive emission to the signal in the in-band filter channels were found by subtracting out the contribution due to Rayleigh scattering and background by means of the equations

$$S_{2P}(3) - S_{\text{total}}(3) - c(3)S(2) \quad (14a)$$

and

$$S_{2P}(0) - S_{\text{total}}(0) - c(0)S(2) \quad , \quad (14b)$$

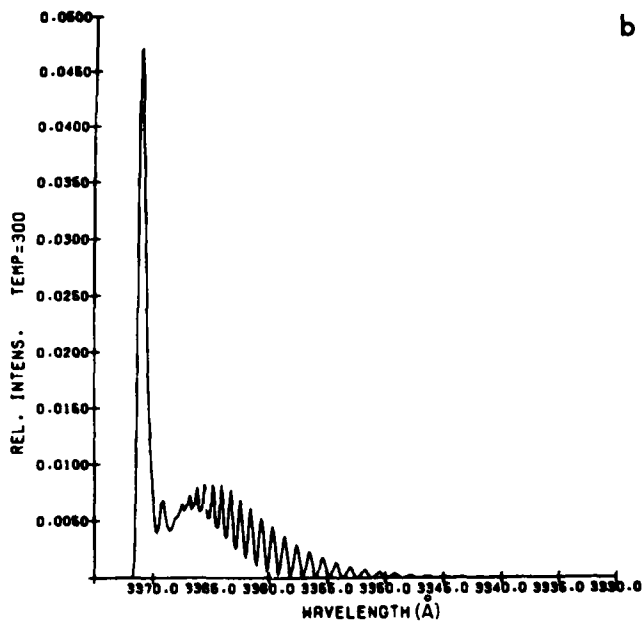
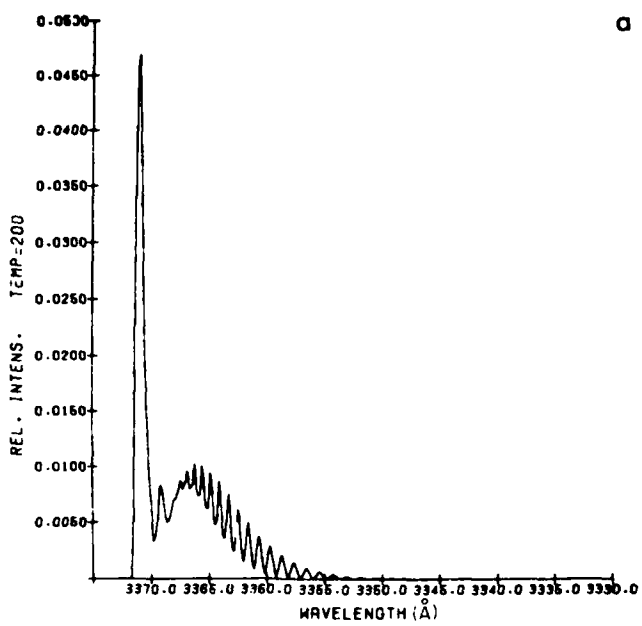


Figure 13. The Spectral Distributions of Intensity of the 3371 Å Band of the  $\text{N}_2$  Second Positive System at Temperatures From 200° to 900°K

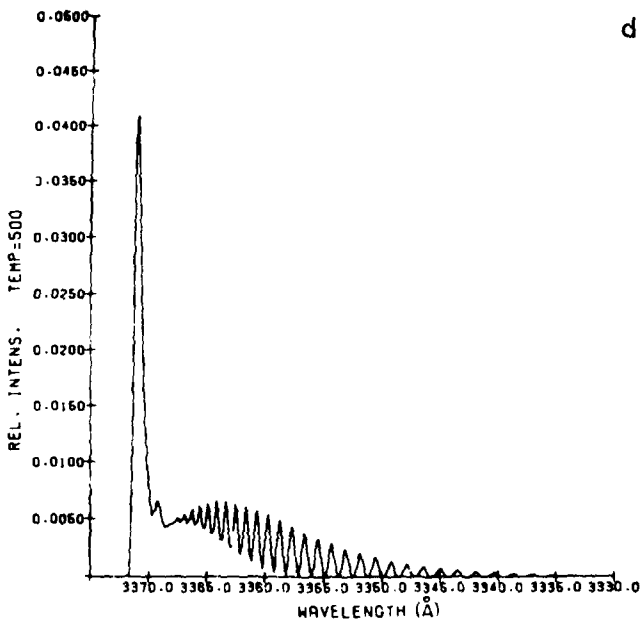
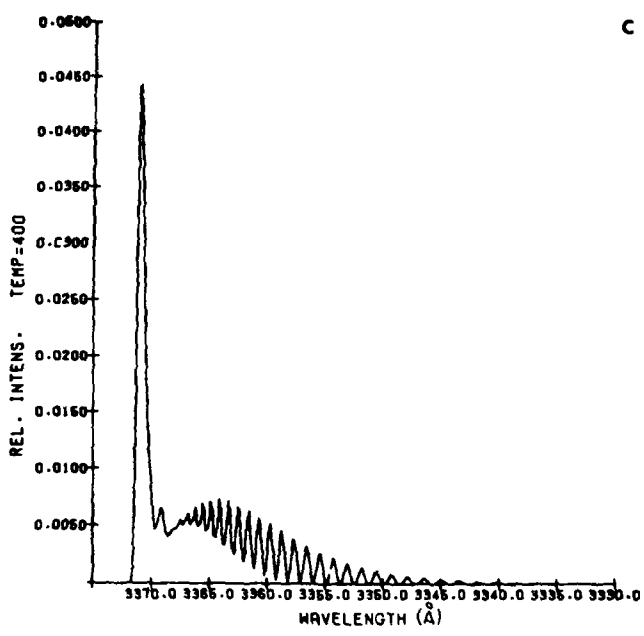


Figure 13. The Spectral Distributions of Intensity of the 3371 Å Band of the  $\text{N}_2$  Second Positive System at Temperatures From 200° to 900°K (Cont.)

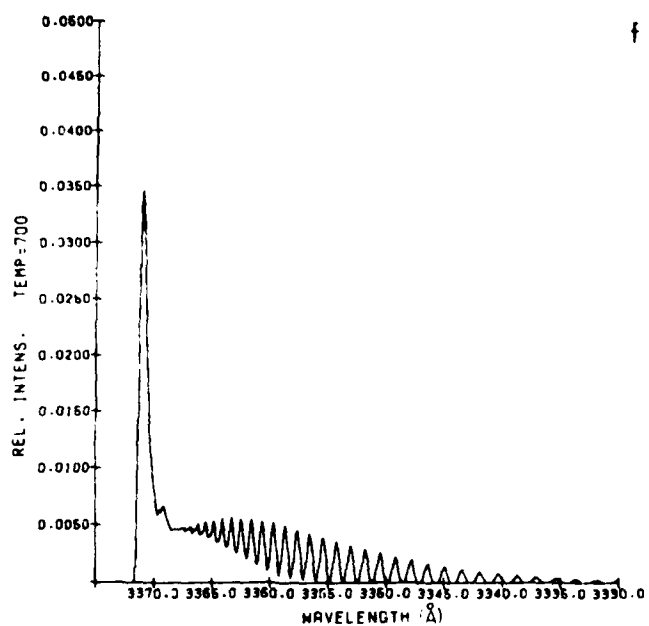
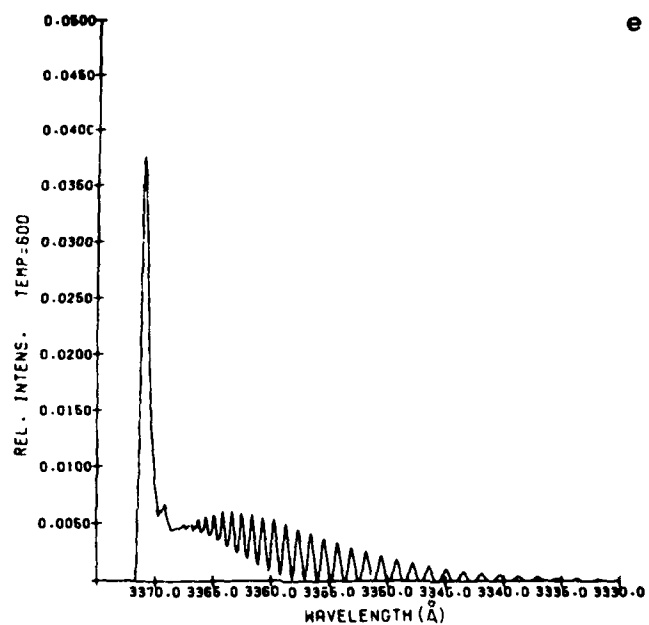


Figure 13. The Spectral Distributions of Intensity of the 3371  $\text{\AA}$  Band of the  $\text{N}_2$  Second Positive System at Temperatures From 200° to 900°K (Cont.)

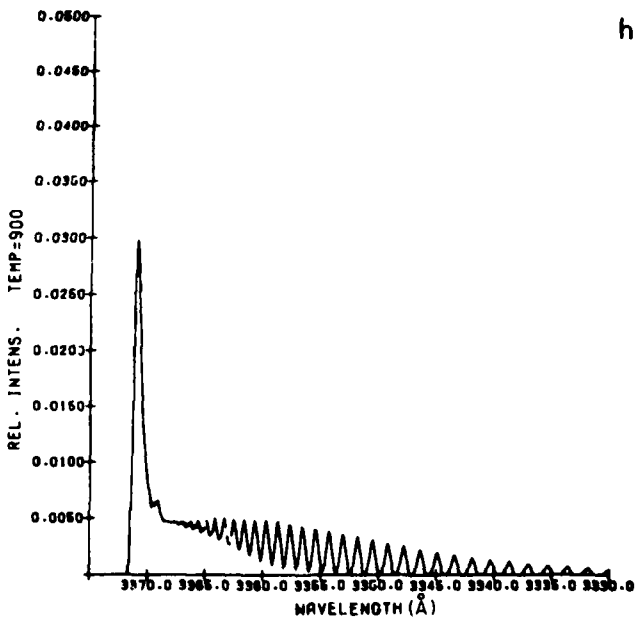
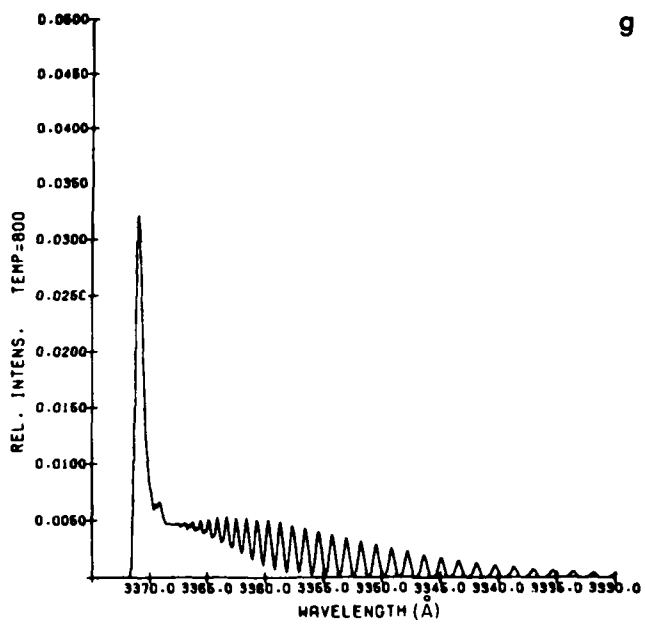


Figure 13. The Spectral Distributions of Intensity of the 3371 Å Band of the N<sub>2</sub> Second Positive System at Temperatures From 200° to 900°K (Cont.)

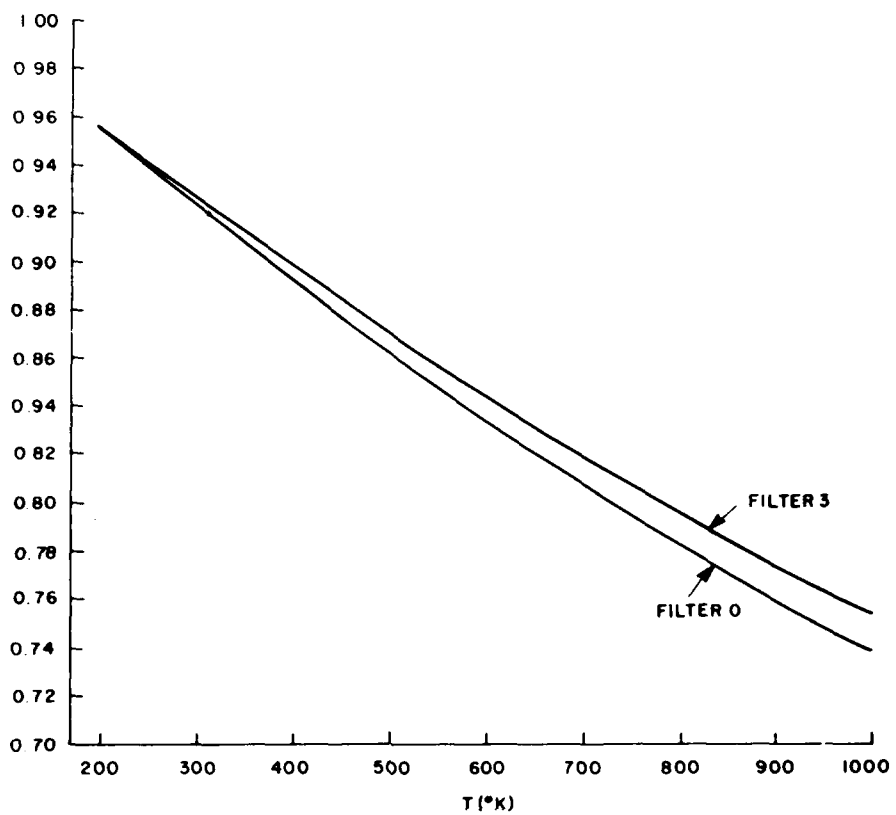


Figure 14. The Relative Band Response for Filter Channels 0 and 3 to the 3371 Å Band of N<sub>2</sub> for Rotational Temperatures Ranging From 200° to 1000°K

where  $S_{2P}$  is the signal due to the second positive emission,  $S_{\text{total}}(n)$  is the total signal in the nth channel, and  $c(n)$  is the proportion of the background signal.

To determine the  $c$  coefficients, we assume that there is no additional contribution to the in-band channels from second positive emission below about 98 km. This is so because the emission is assumed to be produced by electron impact excitation and the solar ultraviolet capable of producing photoelectrons is completely absorbed out below about 98 km.

The resulting values of  $S_{2P}$  are shown in Figures 21 and 22. The signal is shown to flatten at altitudes less than about 98 km.

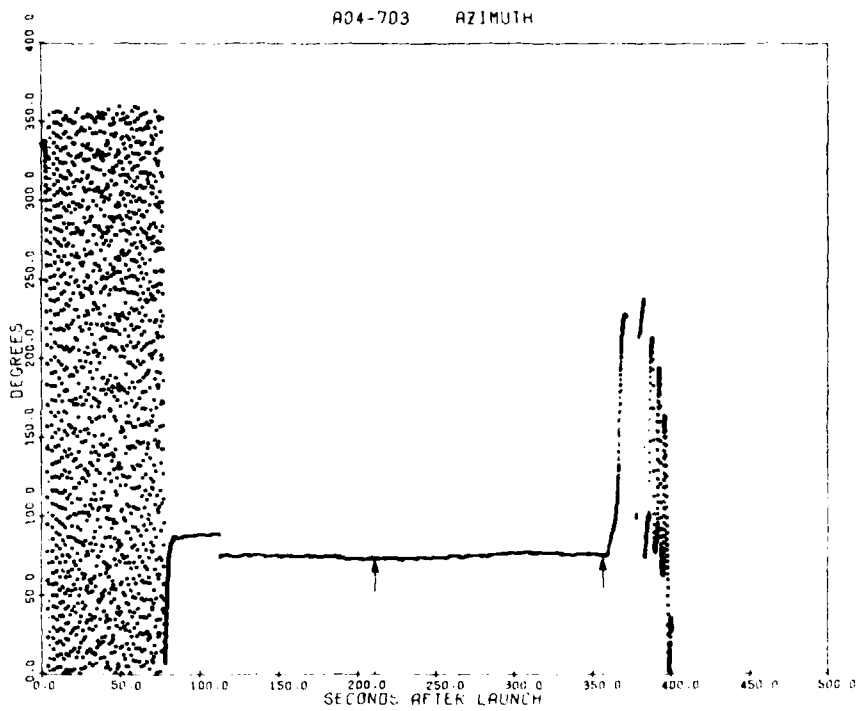


Figure 15. The Elevation of the Photometer During the Flight. The data were taken between the points indicated by the arrows

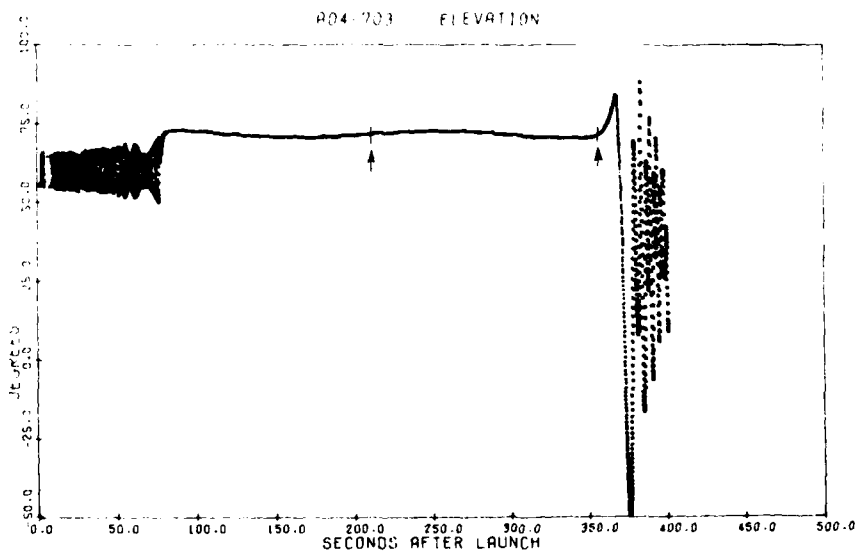


Figure 16. The Azimuth of the Photometer During the Flight. The data were taken between the points indicated by the arrows

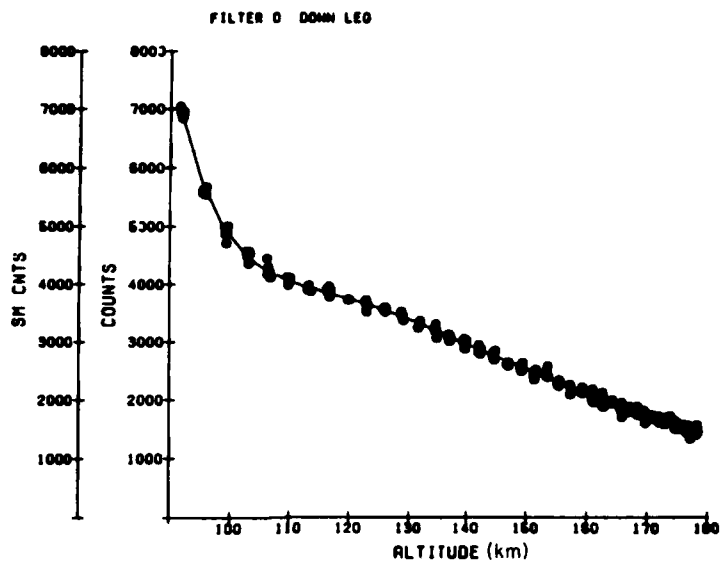


Figure 17. Counts per 100 msec Frame vs Altitude for Channel 0. The solid line indicates the fit to the data

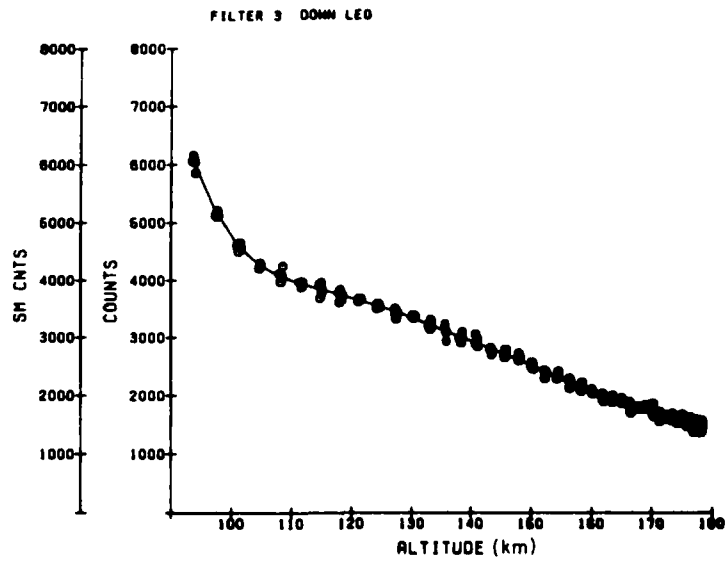


Figure 18. Counts Per 100 msec Frame vs Altitude for Channel 3. The solid line indicates the fit to the data

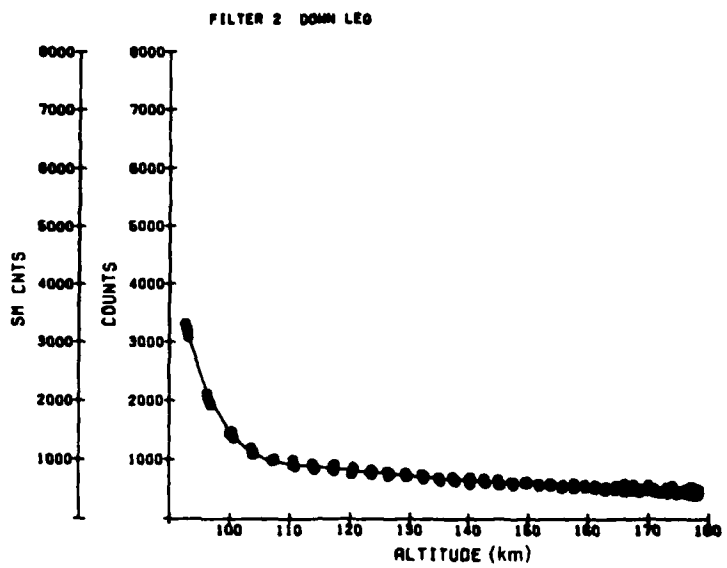


Figure 19. Counts Per 100 msec Frame vs Altitude for Channel 2. The solid line indicates the fit to the data

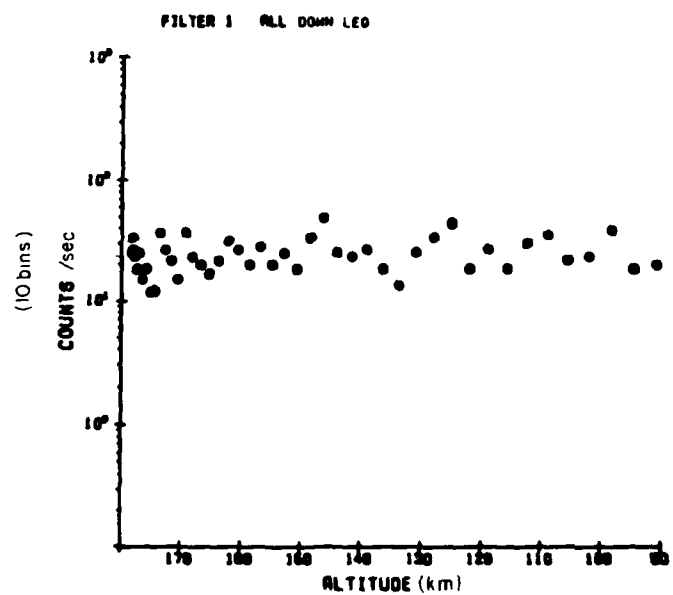


Figure 20. Counts Per 100 msec Frame vs Altitude for Channel 1 (dark count)

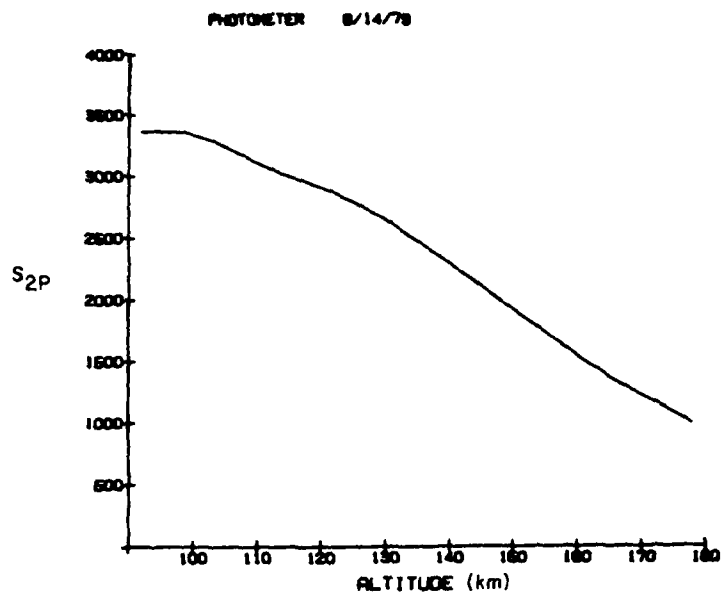


Figure 21. Counts Per 100 msec Frame vs Altitude for Second Positive Emission for Channel 0

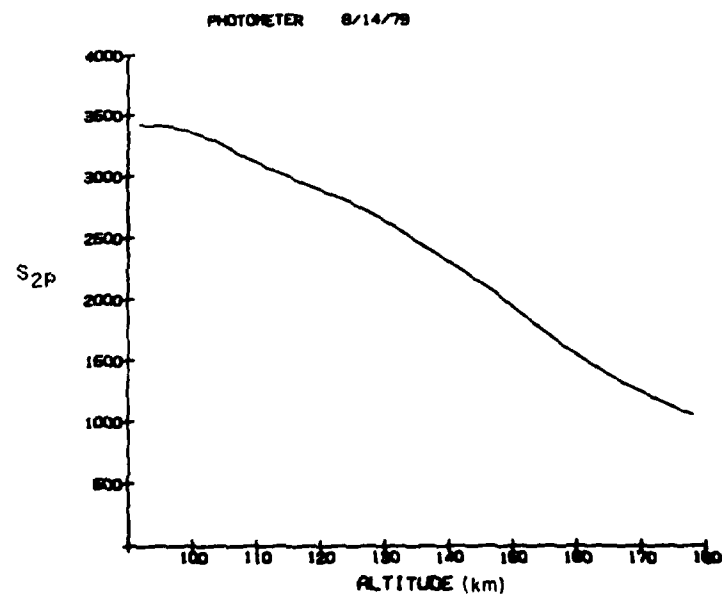


Figure 22. Counts Per 100 msec Frame vs Altitude for Second Positive Emission for Channel 3

#### 5.4.1 VOLUME EMISSION RATE

The second positive volume emission rate,  $J_{2P}(h)$ , is found by differentiating the signal due to second positive emission,  $S_{2P}$ , and applying the calibration factors according to the equation

$$J_{2P}(h) = \left( \frac{dS_{2P}}{dh} \right) \frac{10}{C_0 W_{eq} \int \beta_\lambda(T, \lambda) \eta(\lambda) d\lambda} .$$

The expression in the integral is the relative band response and is a function of the temperature of the neutral atmosphere. This temperature was determined by using the Jacchia model atmosphere described earlier in this paper.

The results for the two channels are given in Figure 23. The average of the two curves is shown in Figure 24.

A clear double peak in the intensity is observed with the major peak about 150 km and another secondary peak at 108 km. Although this secondary peak has not been previously observed, its existence was predicted by Van Tassel<sup>23</sup> on the basis of calculated electron fluxes using detailed computations of Jasperse.<sup>14</sup>

#### 5.4.2 COLUMN EMISSION RATE

If the calibration factor did not contain an altitude-dependent factor through the local temperatures, the column emission rate would be determined directly by applying the calibration factor to the signals due to the second positive emission already shown in Figures 21 and 22. In this case we determine the column emission rate by assuming an average temperature, and hence a value for the relative band response, for the emission above apogee and integrating below that altitude. The column emission rate shown in Figure 25 was calculated by assuming an average relative band response of 0.73 above apogee and integrating the average volume emission rate below apogee.

---

23. Van Tassel, R.A. (1978) Airglow Calculations for Remote Sensing of Density, AFGL-TR-78-0115, AD A057 478.

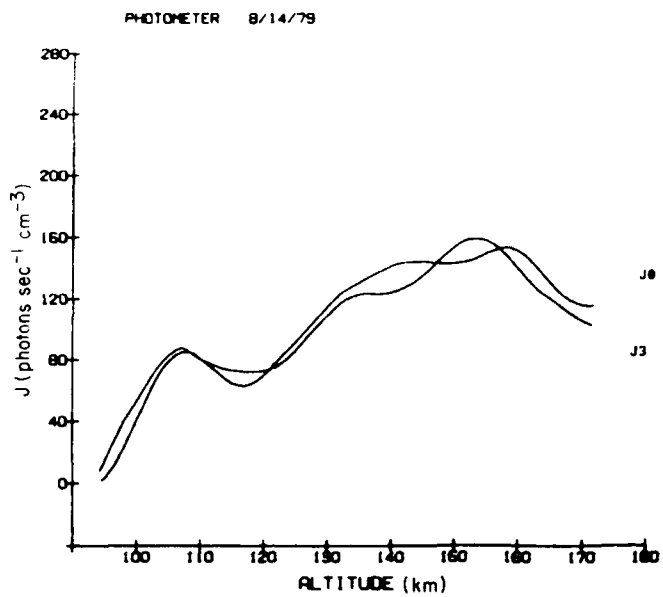


Figure 23. Volume Emission Rate for the  $N_2$  Second Positive (0, 0 band) Emission. The results of the two in-band channels are shown separately

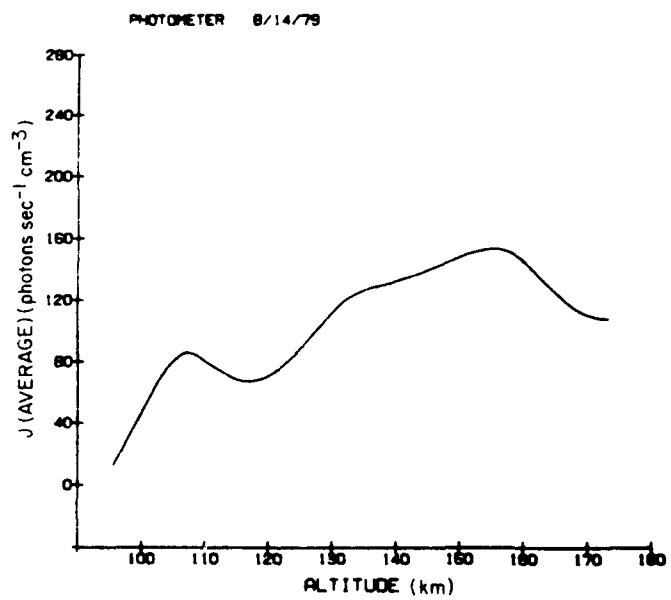


Figure 24. Volume Emission Rate of  $N_2$  Second Positive (0, 0 band)

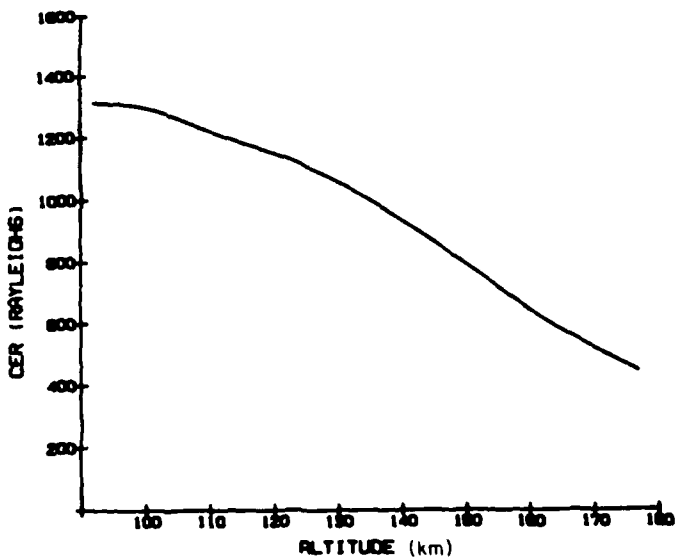


Figure 25. Column Emission Rate of  $N_2$  Second Positive (0, 0 band)

## References

1. Higgins, J. E. (1976) The solar EUV flux between 230 and 1220 Å on November 9, 1971, J. Geophys. Res. 81:1301.
2. Rumsh, M. A., Lukirskii, A. P., and Shchemelev, V. N. (1960) Dokl. Akad. Nauk USSR 135:55 [English translation: Soviet Physics-Doklady 5:1231].
3. Heroux, L., Manson, J. E., Hinteregger, H. E., and McMahon, W. J. (1965) Photoelectric yields for oblique incidence of extreme ultraviolet radiation, J. Opt. Soc. Am. 55:103.
4. Lapson, L. B., and Timothy, J. G. (1976) Channel electron multipliers: detection efficiencies with opaque MgF<sub>2</sub> photocathodes at XUV wavelengths, Appl. Opt. 15:1218.
5. Ederer, D. L., and Tomboulian, D. H. (1964) The performance of a Geiger Mueller counter in the 100-300 Å region, Appl. Opt. 3:1073.
6. Manson, J. E. (1972) Measurements of the solar spectrum between 30 and 128 Å, Solar Phys. 27:107.
7. Manson, J. E. (1973) Light source and filters for use in the 130-280 Å region, Appl. Opt. 12:1394.
8. Jacchia, L. G. (1977) Smithsonian Astrophysical Observatory, Special Report 375.
9. Huffman, R. E. (1969) Absorption cross sections of atmospheric gases for use in aeronomy, Can. J. Chem. 47:1823.
10. Kirby, K., Constantinides, E. R., Babeau, S., Oppenheimer, M., and Victor, G. A. (1978) Harvard-Smithsonian Center for Astrophysics, Preprint Series No. 1018, submitted to Atomic Data and Nuclear Tables.
11. McMahon, W. J., and Heroux, L. (1978) Rocket measurement of thermospheric photoelectron energy spectra, J. Geophys. Res. 83:1390.
12. Doering, J. P., Peterson, W. K., Bostrom, C. O., and Potemra, T. A. (1976) High resolution daytime photoelectron energy spectra from AE-E, Geophys. Res. Lett. 3:129.

13. Victor, G.A., Kirby-Docken, K., and Dalgarno, A. (1976) Calculations of the equilibrium photoelectron flux in the thermosphere, Planet. Space Sci. 24:679.
14. Jasperse, J.R. (1977) Electron distribution functions and ion concentrations in the earth's lower ionosphere from Boltzmann-Fokker-Planck theory, Planet. Space Sci. 25:743.
15. Smith, W.J. (1960) Modern Optical Engineering, McGraw-Hill Book Co., New York.
16. Grum, F., and Luckey, G.W. (1968) Optical sphere paint and a working standard of reflectance, Appl. Opt. 7:2289.
17. Doering, J.P., Fastie, W.G., and Feldman, P.D. (1970) Photoelectron excitation of N<sub>2</sub> in the day airglow, J. Geophys. Res. 75:4787.
18. Coster, D., Brons, F., and Van der Ziel, A. (1933) Die sogenannte zweite positive gruppe des stickstoffspektrums, Z. Physik. 84:304.
19. Huber, K.P., and Herzberg, G. (1979) Molecular Spectra and Molecular Structure, IV. Constants of Diatomic Molecules, Van Nostrand Reinhold Co., New York.
20. Herzberg, G. (1950) Spectra of Diatomic Molecules, Second Edition, D. Van Nostrand Co., Inc., New York.
21. Edlen, B. (1953) The dispersion of standard air, J. Opt. Soc. Am. 43:339.
22. Kovacs, I. (1969) Rotational Structure in the Spectra of Diatomic Molecules, American Elsevier Publishing Co., Inc., New York.
23. Van Tassel, R.A. (1978) Airglow Calculations for Remote Sensing of Density, AFGL-TR-78-0115, AD A057 478.

